Contract No. and Disclaimer:

This manuscript has been authored by Savannah River Nuclear Solutions, LLC under Contract No. DE-AC09-08SR22470 with the U.S. Department of Energy. The United States Government retains and the publisher, by accepting this article for publication, acknowledges that the United States Government retains a non-exclusive, paid-up, irrevocable, worldwide license to publish or reproduce the published form of this work, or allow others to do so, for United States Government purposes.

The Simulation of Fine-Scale Nocturnal Boundary Layer Motions with a Meso-Scale Atmospheric Model

David Werth, Monique Leclerc, Matthew Parker, Nelson Luís Dias, Gengsheng Zhang, Marc Fischer, and Robert Kurzeja

Abstract

A field project over the Atmospheric Radiation Measurement-Clouds and Radiation Testbed (ARM-CART) site during a period of several nights in September, 2007 was conducted to explore the evolution of the low-level jet (LLJ). Data was collected from a tower and a sodar and analyzed for turbulent behavior. To study the full range of nocturnal boundary layer (NBL) behavior, the Regional Atmospheric Modeling System (RAMS) was used to simulate the ARM-CART NBL field experiment and validated against the data collected from the site. This model was run at high resolution, and is ideal for calculating the interactions among the various motions within the boundary layer and their influence on the surface.

The model reproduces adequately the synoptic situation and the formation and dissolution cycles of the low-level jet, although it suffers from insufficient cloud production and excessive nocturnal cooling. The authors suggest that observed heat flux data may further improve the realism of the simulations both in the cloud formation and in the jet characteristics. In a higher resolution simulation, the NBL experiences motion on a range of timescales as revealed by a wavelet analysis, and these are affected by the presence of the LLJ. The model can therefore be used to provide information on activity throughout the depth of the NBL.

1. Introduction

The stable nocturnal boundary layer (NBL) is characterized by a strong inversion and weak turbulent motions. It is during this time that low-level jets (LLJs) often form, usually resulting from the decoupling between the surface conditions with the rest of the atmosphere. This leads to the creation of supergeostrophic winds with flows approaching 15-25m/s at levels below 1000m in the region characterized as the "Great Plains" region of the United States (Jiang et al., 2007). During the daytime, turbulent mixing quickly damps such organized motion, but at night the surface cooling establishes an inversion which reduces turbulence and allows jets to form uninhibited.

The southerly Great Plains LLJ is an important characteristic of the Midwestern boundary layer (generally below 1000m), where it often forms during the period from April to September (Jiang et al., 2007). Its role in moisture transport and mid-level convergence during non-NBL nights makes it a key factor in Midwestern precipitation. Jiang et al. (2007) used a general circulation model (GCM) to demonstrate that the formation of the LLJ is related to both a diurnal oscillation of the pressure gradient force (associated with the greater heating and cooling of the sloping terrain) and the nocturnal damping of turbulence. Interestingly, the characterization of the Great Plains LLJ is important if that area is to be tapped as a source of wind energy, but few examples of mesoscale modeling of the LLJ and subsequent validation exist in the literature (Banta et al., 2008). Storm et al., (2008) simulated a Texas and Kansas LLJ with a 4km-resolution WRF model grid. Overall the model did well, but in both cases the simulated jet core was too high and too weak. This was attributed to problems with the parameterization of vertical mixing. The use of a mesoscale model (Zhong et al., 1996) has also been used to evaluate the

proposed LLJ development mechanisms, and the simulation reproduced several features of the LLJ - the periodicity in wind speed and direction, the level of formation, and the damping of turbulence kinetic energy (TKE) during the active LLJ periods. In the simulations by Zhong et al. (1996), frictional decoupling was found to be more important than the pressure oscillation. That study, along with that of McCorcle (1988), also found soil moisture to be important, with drier soil allowing stronger jets to form.

The properties of the NBL can exert a strong effect on vertical transport. For example, Mathieu et al. (2005) used data from an NBL field project in Ottawa, Canada to show how the LLJ can be interpreted as a 'lid' that inhibits vertical mixing and keeps the CO_2 respired from vegetation confined within a well-defined layer. However, the occurrence of turbulent bursts and the formation of coherent plume structures can lead to the subsequent 'flushing' of CO_2 and other similarly confined tracers upward and away from the surface (Karipot et al., 2006; Cooper et al., 2006; Prabha et al., 2007), so a complicated picture has formed regarding the dynamics of heat and mass within the NBL. This must be well understood in light of the intense monitoring of CO_2 currently underway (Karipot et al., 2008).

Despite its relative stability, the NBL is characterized by turbulence across a range of scales and the turbulence is strongly related to the strength and height of the LLJ (Banta et al., 2003; Prabha et al., 2006; 2007; Smedman et al., 2004). The presence of the jet modulates the spectrum of motions present within the boundary layer. An analysis of data from a field project in Oklahoma (Hong et al., 2008) revealed scales of turbulence measured at 5m above ground level were more or less consistent with Monin-Obukhov theory, in which turbulence varies linearly with height as progressively larger eddies exist. At such a relatively low layer, however, most turbulence is generated by friction with the surface. Turbulent eddies produced at higher

levels can propagate downward into the boundary layer (Prabha et al., 2007), and this process may be affected by the presence of a LLJ (Prabha et al., 2007; Smedman et al., 2004). Indeed, below the LLJ, the turbulent production (caused by the shear) is damped by buoyant motions, but immediately above the LLJ, where the shear is also strong but the stability is weaker, turbulent eddies are produced more easily. These eddies can move below the LLJ into the stable boundary layer, but the LLJ can affect this process preferentially on eddies of different sizes ---- the Smedman mechanism (i.e. the shear-sheltering mechanism) (Prabha et al., 2007).

A field project over the Atmospheric Radiation Measurement-Clouds and Radiation Testbed ARM-CART site during a period of several clear, stable nights was conducted to determine how the NBL varies during its lifecycle. Data was collected from a 10m tower (providing data at a few levels continuously) and a sodar (providing data up to 900m continuously). With data limited to a single location, the full spatial and temporal range of NBL behavior is difficult, if not impossible, to determine. In such cases, however, a model can be used to infer spatial and temporal information of the NBL. With a larger domain, a simulation of the NBL can provide information over extensive spatial (including vertical) and temporal ranges. Constraints on the model eddy size by the grid sizes notwithstanding, a series of smaller, finer nests can provide insight into the eddy motion at relevant scales. If the NBL simulation performs well as compared to observed data, then we can be confident that simulations of the boundary layer motions are reasonably accurate. Model data can then be used to study the turbulent structure at locations in which no data exist. An accurate model of the NBL can allow us to explore motions within the layer which currently go unobserved - particularly at upper levels (above towers), where continuous measurements throughout the night rarely exist.

In the NBL, turbulence is dominated by smaller eddies (as opposed to daytime, when

larger, convective eddies are more prominent) (Beare et al., 2006). Numerical simulations of the NBL are therefore inherently more difficult as a larger share of the turbulence must be calculated by sub-grid scale parameterizations. Overcoming this problem was the goal of the GEWEX Atmospheric Boundary Layer Study (GABLS) study, in which a set of extremely high-resolution experiments was performed to compare LES results for a range of grid spacings (from 12.5m to 1m) for a 400m x 400m domain (Beare et al., 2006). The results demonstrated the benefits of these small grid sizes since much of the turbulent activity was being resolved explicitly. The clock time required to run these simulations was more than a month to produce a nine hour simulation (and only two participating laboratories were able to perform simulations at the 1m resolution), so the practicality of running simulations like this regularly is doubtful at this time. Can we simulate the NBL with a more modest expense of computing power, and what will the quality of the information be? The objective of the present study is, therefore, to demonstrate the applicability of the model to simulate observed boundary layer motions and to examine turbulence structure and transport at scales outside the range of field measurements.

The field project conducted at Lamont, Oklahoma (Hong et al., 2009) in September of 2007 provides a good opportunity to test such a model and see if it can indeed produce a realistic simulation of the NBL, particularly with respect to LLJ formation. The Regional Atmospheric Modeling System (RAMS, Pielke et al. 1992) is used to simulate the period from the field project, and the model data compared to the field data collected at Lamont. The focus of this paper is on the simulation of both the diurnal LLJ lifecycle and the eddy motions that occur within the NBL.

2. Field Experiment

The ARM-CART site is located in Lamont, Oklahoma at 36.616N, 97.5W and was the site of the field experiment during the period from September 10, 2007 to September 24, 2007. Data were collected using three eddy-covariance flux systems using omnidirectional fast-response sonic anemometers/thermometers (Campbell Scient. Inc., Logan, UT) co-located with fast-response open-path CO2 analyzers (Li-Cor, Lincoln, NE) placed at 2, 5, and 10m. The three velocity components (u,v,w), the virtual temperature (Ts), CO_2 concentrations and H_2O concentrations were stored with a data logger (CR-5000, Campbell Scient. Inc., Logan, UT), all at 20Hz. A boundary-layer sodar (Remtech, Paris) was also used to collect continuous data at up to 900m throughout the intensive observation period (IOP).

Additional wind and temperature data from the ARM-CART site was collected at 60m and by other permanent meteorological monitoring assets.

3. Boundary Layer Simulation with RAMS

a. The Model

The Regional Atmospheric Modeling System (Pielke et al., 1992) was used to simulate the nocturnal boundary layer for this experiment. RAMS can be run at high resolution and is ideal for calculating the interactions among the various motions within the boundary layer and their influence on the surface (Buckley and Kurzeja, 1997; Avissar et al., 1998; Gopalakrishnan and Avissar, 2000).

The model solves the non-hydrostatic equations of motion for velocity and potential temperature on a staggered C-grid (Arakawa and Lamb, 1977) with a polar-stereographic projection. A terrain-following sigma coordinate system, in which the bottom of the model

domain follows the terrain, exists in the vertical direction. The model also uses a variable vertical grid spacing in which the layer thickness starts small near the surface and gradually increases with height to a predetermined maximum. In this way, fine-scale motions near the surface can be resolved while allowing for a coarser (and less computationally expensive) vertical resolution aloft, where such motions are less relevant.

The Harrington radiative transfer scheme (Gabriel et al., 1998), which uses a two-stream approximation, is applied to both longwave and shortwave radiation. The Kuo cumulus scheme (Kuo, 1974), in which moisture convergence is converted to convective motion, was selected as the cumulus parameterization for the coarser grids (grids 1 and 2). For the finer grids, a cloud prognostic scheme (Cotton et al., 1986; Meyers et al., 1991) was used. For the surface scheme, which plays a large role in determining model surface fluxes, the LEAF-3 surface scheme was used (Walko et al., 2000) Each grid square is assigned a fraction of each of 21 land surface types (based on USGS 1km AVHRR data),, and each type is assigned its own set of variables (leaf area index, albedo, etc.). The fluxes are calculated for each type individually, then averaged to determine the grid-averaged fluxes.

Within the atmosphere, unresolved eddy transport is accomplished with K-theory. The method used to determine the value of the eddy diffusivity (K) is dependent on the eddy-diffusion scheme selected. For the coarser grids, the Mellor-Yamada scheme (Mellor-Yamada, 1974) is used, by which, the horizontal deformation of the resolved wind field is used to get K.

As the model simulates atmospheric conditions, a simple Newtonian relaxation scheme is applied to nudge the outermost grid (grid 1) towards the predetermined boundary values, while the inner grids are each relaxed towards the boundary values from their respective parent grids in a similar way. The relaxation is applied most strongly at the outermost edge, and the strength

gradually decreases to zero within 5 gridpoints of the boundary. In this way, each grid is constrained near the boundary, but is freer to produce small-scale motions in the interior.

b. Application of RAMS

RAMS simulated the period from 0000Z Sept. 15th to 0006Z Sept. 18th, 2007, with a domain centered over the ARM-CART site in Lamont, OK (36.616N, 97.5W). This period is concurrent with the measured observational data at that site, and several LLJs were observed on these nights. The field data collected during the field experiment serves as the standard for validating the model.

A series of 5 nested grids, with horizontal grid spacings of 32km (25x25), 8km (54x54), 2km (74x74), 500m (150x150), and 125m (50x50) (Fig. 1, grid 5 not shown) were used. The outermost grid is forced by 81km data from the Rapid Update Cycle model (Benjamin, 2004). The vertical spacing for all grids is 30m at the surface, gradually expanding to 1000m above 8000m, and the model extends up to 12.8km. The time step is 60 seconds for the outermost grid. Soil wetness and temperature are initialized everywhere from NCEP reanalysis data (Kalnay et al., 1996). This tended to cause the surface to be too cool and moist during test simulations, however, so soil wetness was reduced by 25% before being used to initialize the model.

Two subsequent simulations were performed with an even finer spatial 6th grid of 32.5m horizontal resolution. Both runs were made for Sept. 17 – one for 0800Z-1230Z (characterized by surface cooling and stability), the other from 1800Z-2230Z (characterized by surface heating and turbulent mixing). The vertical spacing was also altered to increase the number of vertical levels within the boundary layer. At this finer resolution, more of the turbulent eddies that dominate boundary layer motion were resolved.

These simulations of the nocturnal boundary can ideally be used as a proxy for NBL data. Such simulations can be a useful tool for predicting boundary layer motions and the effects upon various tracers in the atmosphere.

.

4. Results

a) Synoptic Conditions

During the simulated period, the Midwest is dominated by a high pressure system the gradually moves east (Fig. 2), with the associated southerly winds and warm advection. At 0Z on the 15th, NCEP reanalysis data show that in northern Oklahoma (Fig. 3a), winds are from the north-northeast, and the temperature is in the low 20s (Kalnay et al., 1996). Grid 1 simulation data compares well to that time (Fig. 3b). By the morning of the 15th (12Z), the high has moved to the east, and winds are from the northeast over most of Oklahoma, turning to the south over west Kansas (not shown). Model winds in Oklahoma are more northerly, and the temperatures are slightly too cool, but the model does capture the strong southerly winds in Kansas. That evening, southerly winds develop as a stationary front forms to the west of the area (Fig. 3c). The model winds also shift to southerly (Fig. 3d), and the model temperature is close to the observed temperature. On the morning of Sept. 16th, the high pressure ridge continued to move east. The winds were still southerly in the observations and the model (not shown), but the model is again slightly too cool.

On the evening of the 16th, the front has passed and southerly winds bring warm air to the area. The model winds and temperatures are similar (Figs. 3e,f). The following morning, temperatures in northern Oklahoma have fallen into the mid-20s, which was captured by the model (not shown). By the end of the day, winds have shifted to a more southeasterly direction,

and temperatures have risen to the mid-30s, again in agreement with the model (not shown). Near the end of the period, a low pressure system moved to the north and generated a line of thunderstorms. The model indicates strong southerly moisture advection at this time (not shown).

The conditions that prevail over the period – high pressure and strong synoptic forcing – are conducive to the formation of a nocturnal low level jet as radiant cooling of the surface establishes an inversion and reduces the drag that turbulent motions exert on winds at the top of the boundary layer. This can be seen more clearly by examining the model boundary layer and comparing it to the ARM-CART data from that time.

b) Simulation of the Nocturnal Boundary Layer

To explore the NBL in more detail, data from grid 5 (125m) is compared to measured data from the field campaign. The focus here is on the formation and dissipation of the LLJ. The model data at the site is compared to the SODAR readings, which provide wind speed and direction up to 900m. On the night of the 14th and into the early morning on the 15th (Fig. 4) the simulated LLJ forms too soon (at about 6Z, compared to 9Z for the sodar), but at about the correct level (300-400m), and the LLJ dissipates at around 14Z on the 15th in both the observation and the model. On the night of the 15th, the downward propagation of the LLJ in both observations and the model is evident, though the model LLJ fails to intensify as it reaches its lowest level (200m). The model winds at 900m also appear a little too strong as compared to SODAR data. The model shows the shift of wind direction from easterly to southeasterly, but some discrepancies exist. For example, the model fails to capture the low-level westerlies from 6-12Z, and the brief shift to westerly winds at 15-17Z is also missed. The unstable boundary

layer also forms later in the model (18Z) relative to the observed period (13Z).

On Sept. 16th (Fig.5), the modeled LLJ initiates at the right time (7Z), but reaches its maximum intensity earlier (at 12Z, compared to 15Z in the observations). The modeled LLJ forms at about the right height (500m), and dissipates on the 16th at the correct time as well (by about 17Z). The LLJ reforms at 1Z the next night, reaching an appropriate intensity but forms a little higher in the model (at 500m, compared to 300m in the observations). The jet-level wind arrows indicate that the observed shift from southwesterly to southerly occurs in the model as well.

On Sept. 17th (Fig. 6), the LLJ forms shortly after midnight, and the core lies at 350m. The model LLJ starts and ends at the correct times, but forms slightly higher at about 500m. Like the LLJ of the 17th, the LLJ of the 18th occupies a deep layer (though partially obscured above 400m by missing data in the SODAR). The model LLJ has this characteristic as well, but does not develop a distinct core at 200-300m as seen in the SODAR. The wind arrows show how the model captures the southwesterly winds shifting to southeasterly at 200-500m, but does not capture the stronger southeasterly component above this layer.

Ultimately, the meteorological conditions aloft are linked to conditions at the surface. Near the surface (5m), for example, RAMS data is warmer on all three days (Fig. 7a), though modeled temperature data are accurate at night. At 60m (Fig. 7b), we see the daytime highs are reasonably accurate, but the nighttime lows are slightly cooler, especially on the third night. The 5m winds are weaker (Fig. 8a), particularly on the second day, and the model does not completely capture the intensity of the daytime winds at the surface and aloft (Fig. 8b) on the second day. The model water vapor (Fig. 9) is very close to the observations at all times, suggesting that the model evapotranspiration (which represents a strong control on the surface

heat transfer and the consequent turbulent mixing) is accurate.

A comparison of the surface radiant fluxes (Fig. 10) shows that the model shortwave flux is reasonably accurate, but it appears that the observed data is responding to clouds that the model does not produce. The model is likely emitting too much longwave radiation, which may explain the excessive nocturnal cooling aloft. This aspect is again likely related to insufficient cloud development in the model.

On synoptic scales, the model does well, capturing the temperature changes and shifting winds associated with the departing high pressure system. On the scale of the boundary layer, the model can simulate the cycle of LLJ formation and dissipation, though errors exist in the details of intensity timing and location. The turbulent motions that characterize the boundary layer, however, cannot be resolved with the 125m resolution of grid 5. If we wish to study these motions, we must go to a finer scale.

c) Simulation of Turbulence

The high-resolution (grid spacing = 32.5m) simulation was performed to capture model behavior during the periods of maximum atmospheric stability (between the black arrows on Fig. 6) and maximum observed turbulence (between the green arrows on Fig. 6). At the former time, the jet is strongest, and will therefore exert its strongest effect on the model eddy dynamics. A model sounding from 10Z (Fig. 11) clearly shows the nocturnal temperature inversion, which reaches an inflection point at about 400m. It is above this point that the jet reaches its maximum speed and the 'nose' develops. Above about 800m, we see the jet weakening as temperatures fall with height and thermal stability is no longer exerting a damping effect on the production of eddy motion through shear.

We may suppose that the period of the NBL is characterized by weak turbulence until sunrise initiates surface heating. Turbulence is damped when the Richardson number exceeds 0.25, and this does not occur in the vertical until about 250m aloft (Fig. 12). Some turbulent motions may exist below this level, while the damping of motions above this level is likely (thereby insulating the LLJ).

Fig. 13 shows the nocturnal temperature and wind speed generated by RAMS and field observations, both at 60m. The observed data show mixed long and short period frequencies. Specifically, a steady diabatic cooling occurs throughout the night (Fig. 13a), and wind observations exhibit slow modes of low-amplitude variability, with superimposed turbulent modes, and a gradual slowing trend (Fig. 13b). For the temperature, both RAMS and the observations show a steady cooling, but the observed data shows much greater variability at short timescales (and the model data has a cool bias throughout the period). The wind speed time series also show that the observed data varies over a much greater range at all timescales (covering a range from 6-14m/s, compared to 10.3-10.6m/s in the model), but the dominant timescale appears to be the same. Fig. 14 shows the same comparison for the daytime, when turbulent motions are much stronger. Now, the model temperature is closer to the observations in overall magnitude (both climb from 27.5C to 30-31C during the period), and the model windspeed varies from 10-13 m/s, near the low end of the 11-15m/s range in the observations.

The power spectrum of the wind speed time series can reveal more about the timescales on which both the model and the observations vary. The nighttime and daytime spectra for both the model and the observation time series (Fig. 13b and 14b) are calculated. For the observational time series, the larger variability means that nonstationarity can distort the power spectra. Therefore, the observed time series is first divided into four 256-point series (using only the first

1024 points), and the spectrum calculated for each. The four spectra are then averaged to get a single, representative spectrum. (For the model time series, the 1-minute data means that the entire 4.5 hour series is little longer than 256 points, so only a single spectrum is calculated.) All 4 spectra are then bin-averaged (using 44 bins, each with an equal frequency range) to further smooth out the noise in the spectra, and the results are seen in Fig. 15.

The spectra all adhere roughly to a -5/3 power spectrum. The observed spectra are similar for daytime and nighttime, with less power at lower frequencies during the nighttime. In the model, both spectra exhibit less power than the observed data except at the lowest frequencies (which the model is best at resolving). Unlike the observations, the model nighttime spectrum has much less power than during the day, and variability at all timescales, not just longer periods, is damped at night. Also of note, the daytime spectrum has a 'gap' at 8.0×10^{-4} Hz, corresponding to a spatial scale of 15.150km (applying the mean wind speed of 12m/s). This puts the gap near the upper boundary of the meso-γ scale (Orlanski, 1975) – the scale of convective cells.

Figs. 13-15 show that the high-resolution model cannot capture the full variability observed at the shorter time scales. The spectrum in Fig. 15 does show, however, that some variability does exist at all resolved scales, and that the model turbulence does follow an expected distribution, implying that the simulated interaction between eddies (and the consequent cascade from large to small scales) is occurring in a realistic way. Therefore, the model variability that does exist can still be used to tell us about nocturnal boundary layer turbulent activity.

How is the model variability within the NBL affected by the LLJ, in which strong shear maintains a balance with strong thermal damping? Does the timescale of an eddy or its height affect the way it responds to the presence of the jet? We can explore this by applying a wavelet analysis to the nocturnal timeseries of wind speed at different levels. Wavelet analysis has

proven very useful in the analysis of boundary layer motions (Prabha et al., 2007), as it can identify modes of variability that persist for short periods, and nonstationarity is another prominent characteristic of the NBL.

Wavelet analysis is applied to data at 60m (Fig. 13b,14b), and compared to the results from the same analysis applied to observational data. Before the wavelet analysis is applied, the data are first detrended by subtracting the linear trend, calculated over the entire 4.5-hour series from the original data. This will prevent the trend from appearing as an unphysical low-frequency oscillation in the wavelet spectra. After detrending, the wavelet analysis is applied, and the results are presented in Fig. 16a-d.

As expected, the temperature variability is two orders of magnitude greater in the observed data (Fig. 16a) than in the model (Fig. 16b) due to much more variability at high frequencies. The dominant observed variability lies between 12 minutes to 2 hours, while the model timescales are close at 20 minutes and 2 hours. The model variability maximum lies at about 1 hour, while the observed data peaks at about 40 minutes, again favoring shorter periods. For the wind speed (Figs. 16c, d), we again see the expected orders of magnitude difference in the variability. Both the model and the observations show 2 maxima in the variability – a prominent peak at one at 1 hour, and a second, weaker 'bump' at about 30 minutes. Overall, while the model variability is much smaller, the model is capturing much of the observed timescales of variability.

This same analysis can be applied to time series at other model levels. We select 4 levels – the surface, 164m, 279m, and 904m. These levels all lie within the NBL except 904m, which lies above the LLJ (Fig. 6). By applying the same wavelet analysis, we can determine how the proximity to the LLJ affects the modeled turbulence. As before, the linear trend is

removed from each time series. Then, a time-filter is applied to examine separately the effects on turbulent and slowly-varying motions. A 30-minute running average is applied to the time series of wind speed at several levels to get the low-frequency (LF) component. Then the LF series is subtracted from the original time series to get the high-frequency (HF) component.

At the surface (Fig. 17a), two peaks are apparent at 50 minutes and another, weaker 'bump' at around 23 minutes. At 164m (Fig. 17b), the same peaks exist, but now the longer-period peak has diminished so that the two appear with equal magnitude, with a small gap in between. At 279m, just below the LLJ, the longer-period peak has disappeared, leaving only the single, shorter-period peak (Fig. 17c). Above the jet (Fig. 17d), however, this peak disappears, and the lower-period peak has returned, suggesting that more low-frequency activity is generated at this level.

At higher frequencies, the surface (Fig. 18a) again sees two small peaks, one at 8 minutes, and a second at 22 minutes (overlapping the LF peak). As noted previously the short-period activity is produced by surface friction. Away from the surface, a peak at 22-minutes becomes more prominent as higher frequency activity is damped (Fig. 18b, c), although the spectrum remains fairly broad at 279m relative to the LF spectrum at this level (compare Fig. 17c to Fig. 18c). It appears that the upper level NBL is an area that damps, or inhibits the advection of, the largest eddies, while the smallest eddies are damped by thermal stability except near the surface. (Similar behavior is seen in the temperature wavelet analysis (not shown)). Above the LLJ, a peak at about 11 minutes exists as thermal damping is no longer able to offset the production of the shear-produced high-frequency activity.

5. Conclusions

Fine-scale simulations of the NBL have demonstrated that a numerical mesoscale model (RAMS) can accurately simulate the behavior of the nocturnal boundary layer, including its formation and eventual dissipation. The model high frequency variability was lower than observations indicated, but we could still discern many of the relevant motions within the boundary layer.

There are three benefits that can be drawn from a model of the NBL. First, the model data can serve as a proxy for measurements in the actual BL, and can help us validate theories on BL behavior. For example, the variation of the motion spectra with height can tell us how the LLJ affects eddy motion. Second, the model can be used to elucidate BL behavior in a particular area before a CO_2 or other such monitoring site is established in that area. More so than existing analysis data (such as the NCEP reanalysis), the model can provide guidance on the strength of the LLJ and the timing of its formation - both of which are useful in interpreting the results from field experiments and long-term monitoring projects. This is important as the NBL may be particularly sensitive to changes in radiative forcing (Cava et al., 2004; Walters et al., 2007), so its behavior can vary greatly even during periods of seemingly unvarying larger-scale forcing. Third, the model can theoretically be used to fill-in missing or erroneous data from NBL field projects (the 'gap-filling' procedure, (Baldocchi, 2008)), either by using the existing field data as a 'nudging' with the model, or through the use of a ensemble Kalman filter. We will continue to improve our model, particularly with respect to the high-frequency nocturnal variability, and hope to apply this model to our own future research in NBL behavior.

Acknowledgements

This work was sponsored by the DOE Office of Science – Terrestrial Carbon Processes Program. Select data were obtained from the Atmospheric Radiation Measurement (ARM) Program sponsored by the U.S. Department of Energy, Office of Science, Office of Biological and Environmental Research, Environmental Sciences Division.

6. References

Arakawa, A. and R. V. Lamb, 1977: *Computational design of the basic dynamical processes of the UCLA general circulation model.* Vol. 17, *Methods in Computational Physics*, Academic Press, pp. 174-265

Avissar, R., E.W. Eloranta, K. Gürer, and G.J. Tripoli, 1998: An Evaluation of the Large-Eddy Simulation Option of the Regional Atmospheric Modeling System in Simulating a Convective Boundary Layer: A FIFE Case Study. *J. Atmos. Sci.*, **55**, 1109–1130.

Baldocchi, D., 2008: 'Breathing' of the terrestrial biosphere: lessons learned from a global network of carbon dioxide flux measurement systems, Aus. Jour. Bot., 56, 1-26

Banta, R.M., Y.L. Pichugina, and R.K. Newsom, 2003: Relationship between Low-Level Jet Properties and Turbulence Kinetic Energy in the Nocturnal Stable Boundary Layer. *J. Atmos. Sci.*, **60**, 2549–2555.

Benjamin, S.G., D. Dévényi, S.S. Weygandt, K.J. Brundage, J.M. Brown, G.A. Grell, D. Kim, B.E. Schwartz, T.G. Smirnova, T.L. Smith, and G.S. Manikin, 2004: An Hourly Assimilation–Forecast Cycle: The RUC. *Mon. Wea. Rev.*, **132**, 495–518.

Buckley, R.L., and R.J. Kurzeja, 1997: An Observational and Numerical Study of the Nocturnal Sea Breeze. Part I: Structure and Circulation. *J. Appl. Meteor.*, **36**, 1577–1598.

Cava, D., U. Giostra, M. Siqueira and G. Katul, 2004: Organised Motion and Radiative Perturbations in the Nocturnal Canopy Sublayer above an Even-Aged Pine Forest,, Boundary Layer Meteorology, **112**, 129-157

Cooper, D.I., M.Y. Leclerc, J. Archuleta, R. Coulter, E. W. Eichinger, C. Y. J. Kao and C. J. Nappo. 2006. Mass Exchange in the Stable Boundary Layer by Coherent Structures. Special Issue 'Advances in Surface-Atmosphere Exchange - A Tribute to Marv Wesely'. Agricultural and Forest Meteorology. 136 (3-4): 114-INVITED

Cotton, W. R., Tripoli, G. J., Rauber, R. M., Mulvihill, E. A.,1986: Numerical simulation of the effects of varying ice crystal nucleation rates and aggregation processes on orographic snowfall. *J. Climate Appl. Meteor.,* 25, 1658-1680.

Gabriel, P., J. Harrington, G. Stephens, and T. Schneider, 1998: Adjoint Perturbation Method Applied to Two-Stream Radiative Transfer, *J. Quanr. Specfrosc. Radiot. Transfer,* **59***, Nos 112,* 1-24

Gopalakrishnan, S.G., and R. Avissar, 2000: An LES Study of the Impacts of Land Surface Heterogeneity on Dispersion in the Convective Boundary Layer. *J. Atmos. Sci.*, **57**, 352–371.

Hong, J., M. leclerc, and N. Dias, 2009: Surface-Layer Scaling for Nocturnal Turbulence in an Evolving Low-Level Jet, in preparation

Jiang, X., N.-C. Lau, I. Held, and J. Ploshay, 2007: Mechanisms of the Great Plains Low-Level Jet as Simulated in an AGCM, *J. Atmos. Sci*., **64**, 532-547

Kalnay, E., M. Kanamitsu, R. Kistler, W. Collins, D. Deaven, L. Gandin, M. Iredell, S. Saha, G. White, J. Woollen, Y. Zhu, A. Leetmaa, R. Reynolds, M. Chelliah, W. Ebisuzaki, W. Higgins, J. Janowiak, K. Mo, C. Ropelewski, J. Wang, R. Jenne, and D. Joseph, 1996: The NCEP/NCAR 40-Year Reanalysis Project. *Bull. Amer. Meteor. Soc.*, **77**, 437–471.

Karipot, A., M.Y. Leclerc, G. Zhang, T. Martin, G. Starr, D. Hollinger, J. H. McCaughey, and G. R. Hendrey. 2006. Nocturnal $C0_2$ Exchange Over a Tall Forest Canopy Associated with Intermittent Low-Level Jet Activity. **85(3-4),** *J. Theor. Appl. Climat.* 243-248.

Kuo, H., 1974: Further studies of the parameterization of the influence of cumulus convection on large-scale flow. *J. Atmos. Sci*., **31**, 1232-1240.

Mathieu N., I.B. Strachan, M.Y. Leclerc, A. Karipot, E. Pattey. 2005: Role of low-level jets and boundary-layer properties on the NBL budget technique. **135***, Agr.and Forest Meteorol*. 35-43.

Mccorcle, M.D., 1988: Simulation of Surface-Moisture Effects on the Great Plains Low-Level Jet. *Mon. Wea. Rev.*, **116**, 1705–1720.

Mellor G. L., and T. Yamada, 1974: A hierarchy of closure models for planetary boundary layers, *J. Atmos. Sci.,*. **31**, 1791-1806

Meyers, M. P., DeMott, P.J., Cotton, W.R., 1992: New primary ice nucleation parameterizations in an explicit cloud model. *J. Appl. Meteor.,* 31, 708 721.

Orlanski, I., 1975: A Rational Subdivision of Scales for Atmospheric Processes. *Bull.Amer. Met. Soc*., **56**, 527-530

Pielke R. A., W. R. Cotton, R. L. Walko, C. J. Tremback, W. A. Lyons, L. D. Grasso, M. E. Nicholls, M. D. Moran, D. A. Wesley, T. J. Lee, and J. H. Copeland, 1992: A comprehensive meteorological modeling system--RAMS. *Meteor. Atmos. Phys*., 49, 69-91.

Prabha, T., M. Leclerc, A. Karipot, D. Hollinger, and E. Mursch-Radlgruber, 2007: Influence of Nocturnal Low-level Jets on Eddy –covariance Fluxes over a Tall Forest Canopy, *Bound.-Lay. Met*., **126**, pp. 219-336

Smedman, A., J. Hunt and U. Högström, 2004: Effects of shear sheltering in a slightly stable atmospheric boundary layer with strong shear. *Quart. J. Roy. Meteorol. Soc.,* **130**, 31-50

Walko, R.L., L.E. Band, J. Baron, T.G.F. Kittel, R. Lammers, T.J. Lee, D. Ojima, R.A. Pielke, C. Taylor, C. Tague, C.J. Tremback, and P.L. Vidale, 2000: Coupled Atmosphere–Biophysics–Hydrology Models for Environmental Modeling. *J. Appl. Meteor.*, **39**, 931–944.

Walters, J. T., R. T. McNider, X. Shi, W. B. Norris, and J. R. Christy (2007), Positive surface temperature feedback in the stable nocturnal boundary layer, Geophys. Res. Lett., 34, L12709, doi:10.1029/2007GL029505.

Zhong, S., J. Fast, and X. Bian, 1996: A Case Study of the Great Plains Low-Level Jet Using Wind Profiler Network Data and a High-Resolution Mesoscale Model, *Mon. Wea. Rev*., **124**, 785-806

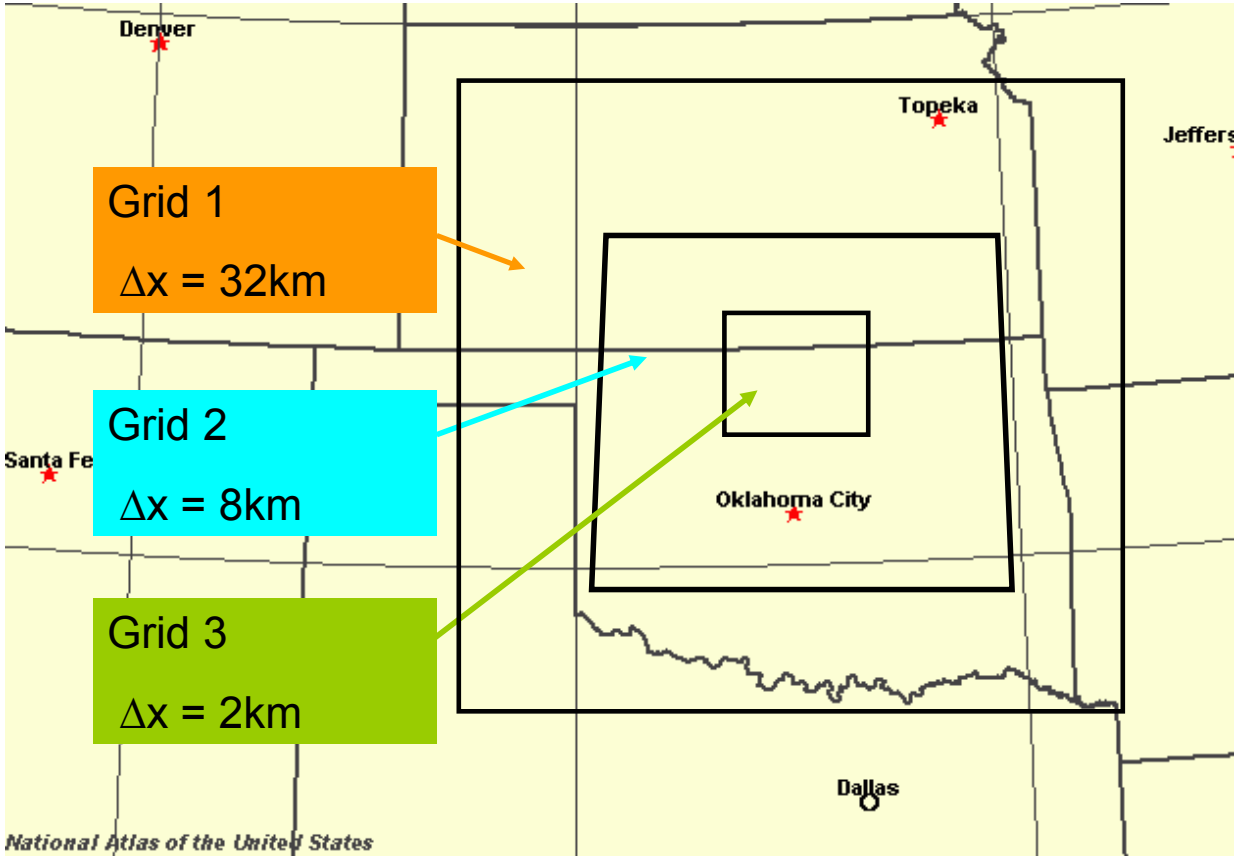

Figure 1a Grids 1-3 used in the RAMS simulations.

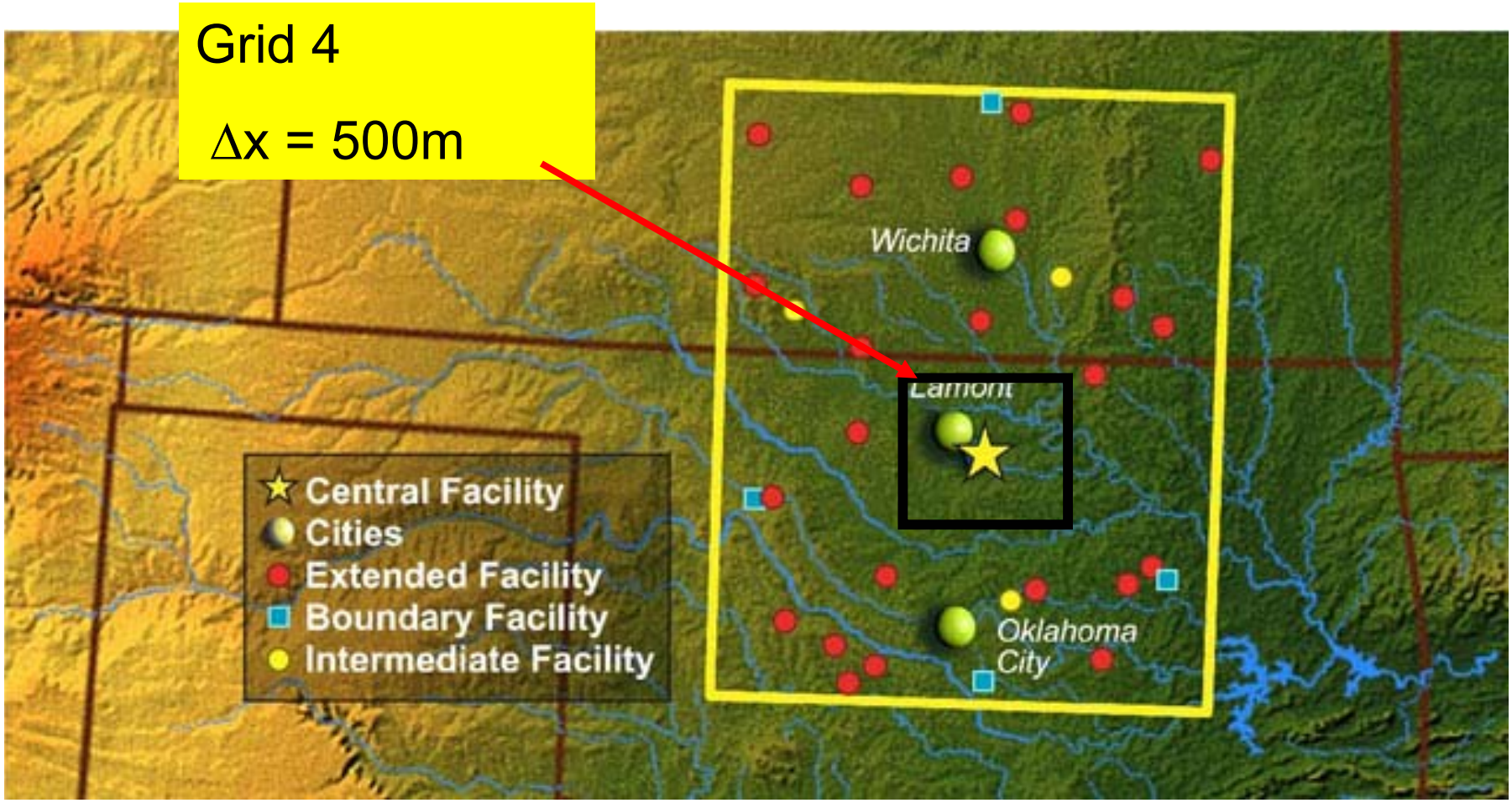

Figure 1b As in Fig. 1a but for grid 4.

a)

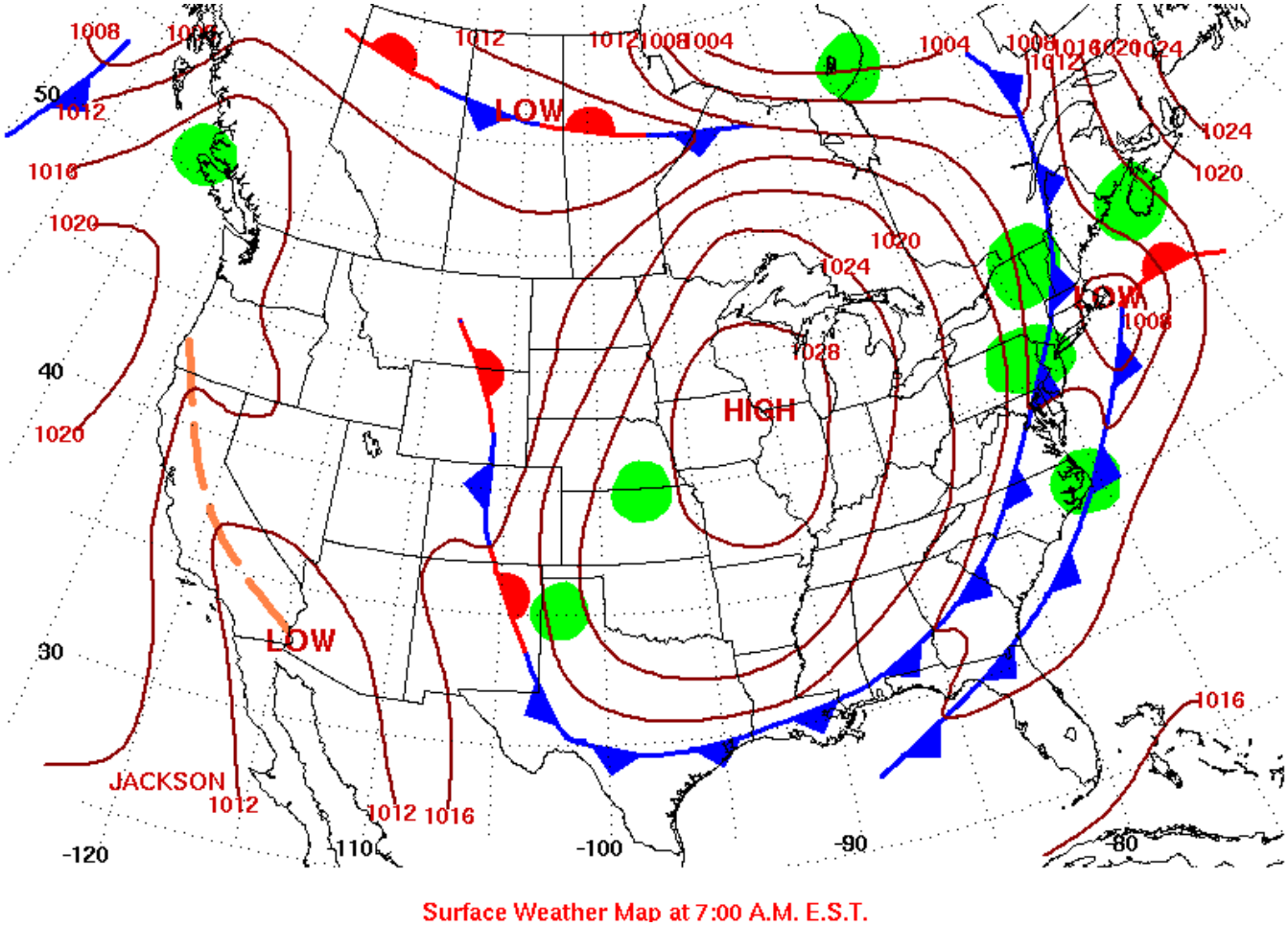

Fig. 2 Synoptic maps for a) 12Z, Sept. 15th, b) 12Z, Sept. 15th, c) 12Z, Sept. 15th, d) 12Z, Sept. 15th

b)

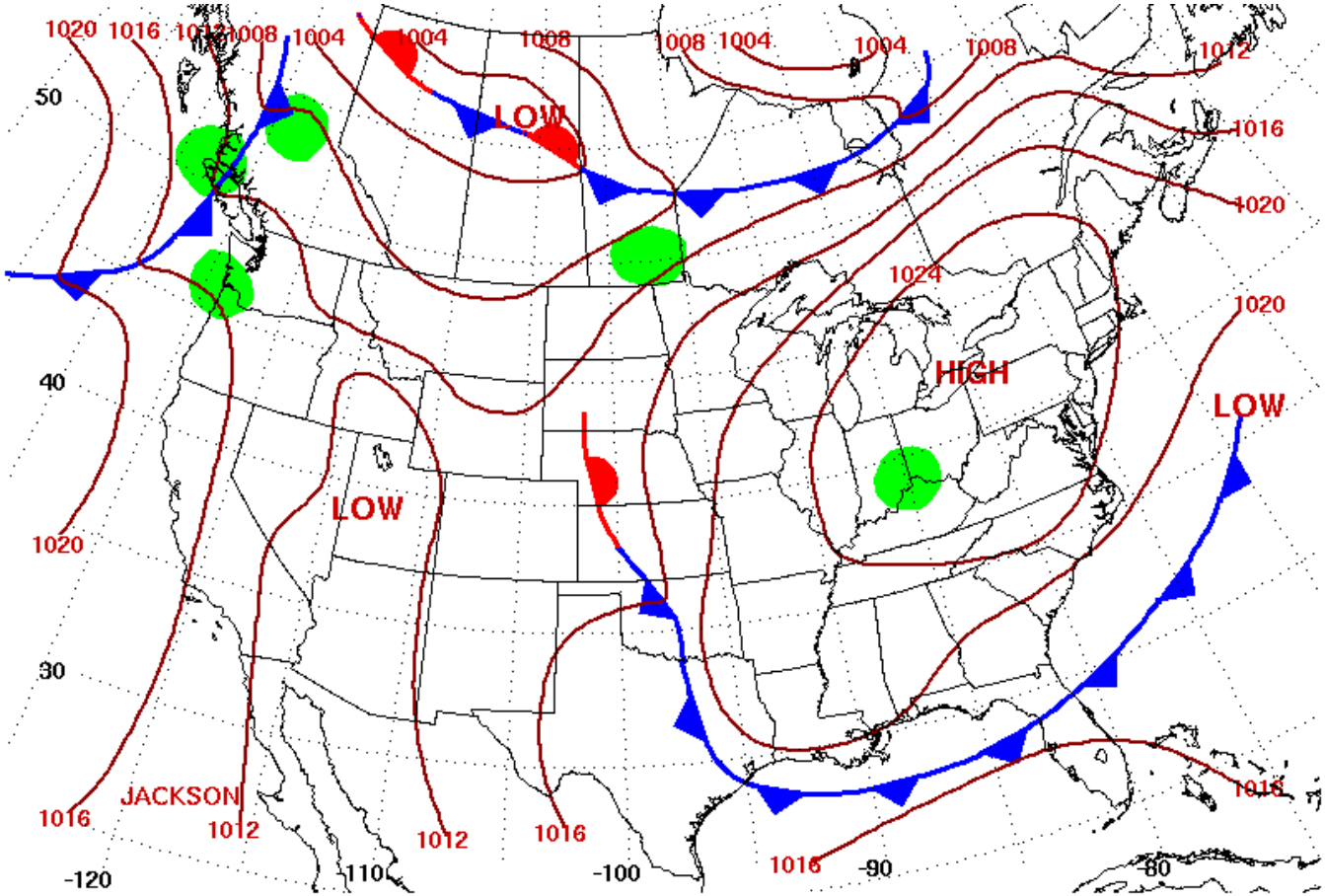

Surface Weather Map at 7:00 A.M. E.S.T.

c)

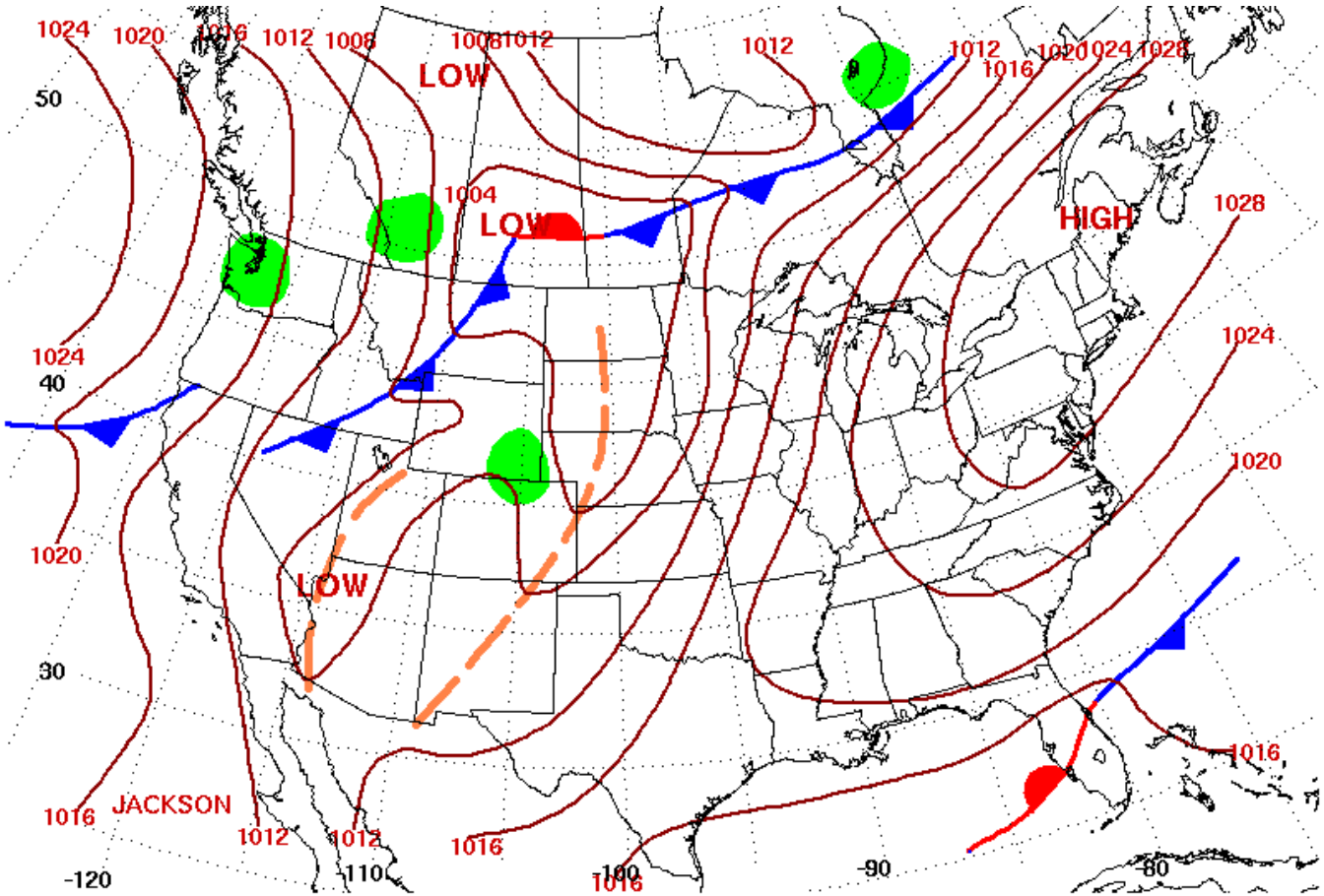

Surface Weather Map at 7:00 A.M. E.S.T.

d)

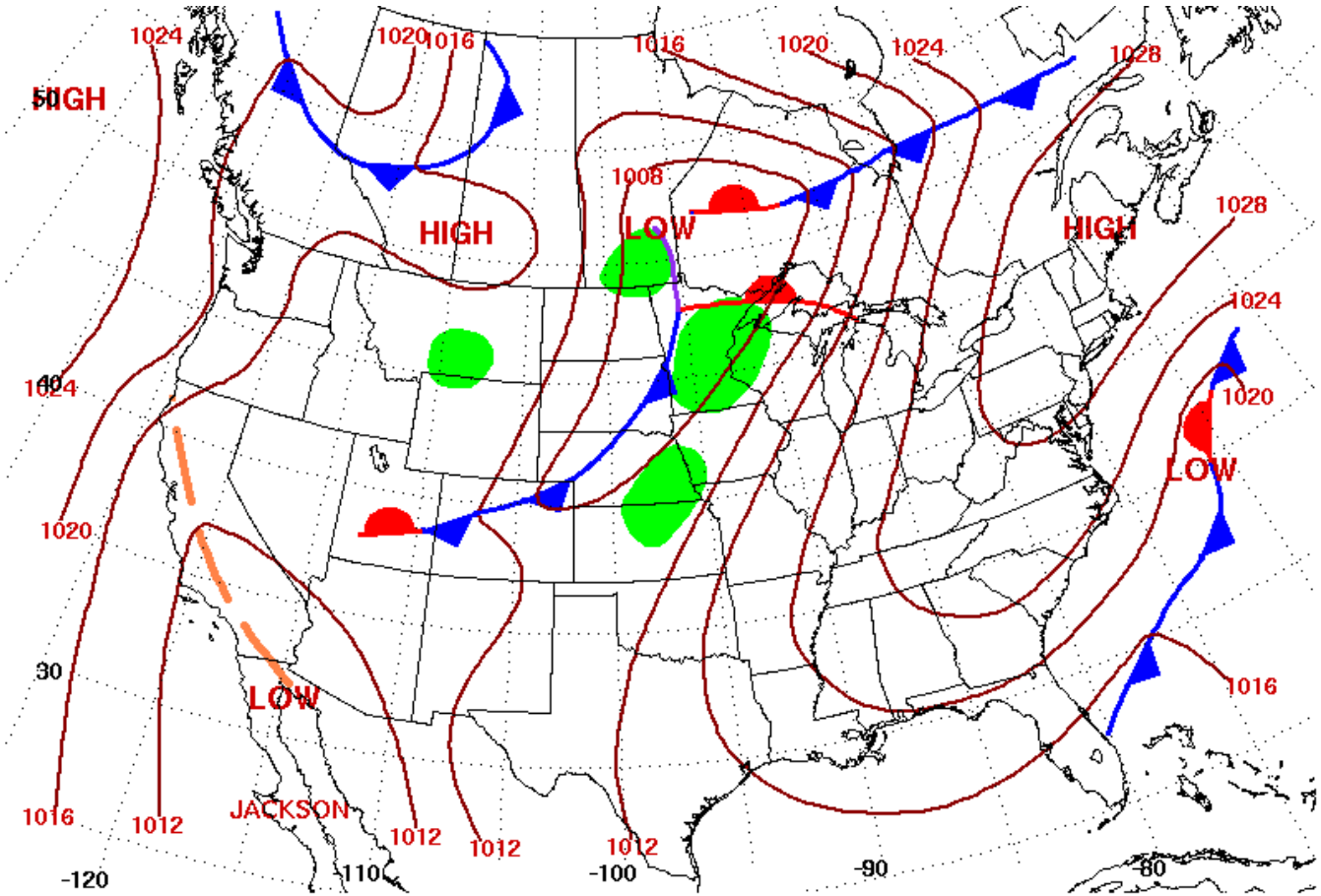

Surface Weather Map at 7:00 A.M. E.S.T.

a

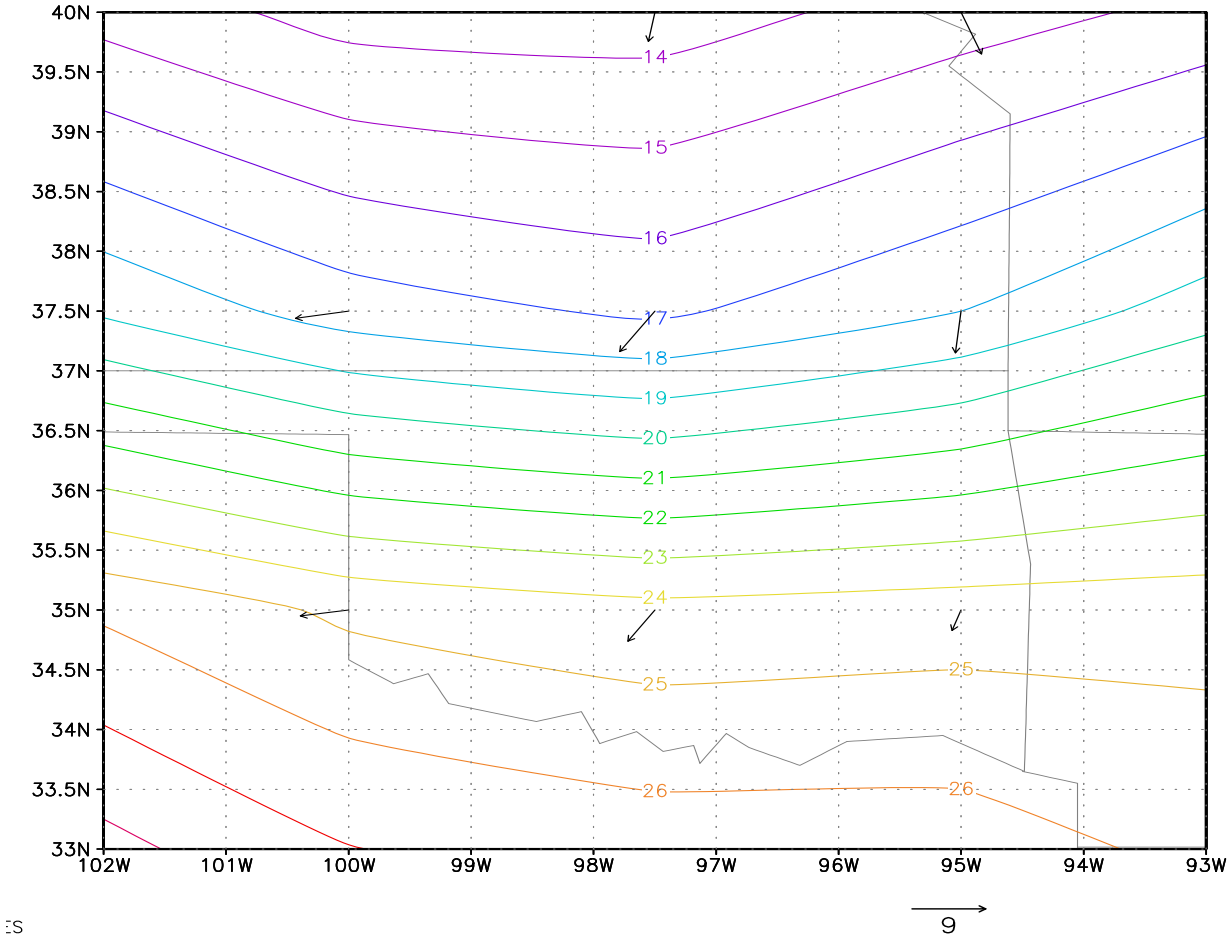

Fig. 3 Synoptic surface temperatures (contours) and winds (vectors) during the period from a) NCEP Reanalysis at Sept. 15, 0Z, b) RAMS at Sept. 15, 0Z, c) NCEP Reanalysis at Sept. 16, 0Z, d) RAMS at Sept. 15, 0Z, e) NCEP Reanalysis at Sept. 17, 0Z, f) RAMS at Sept. 17, 0Z

b

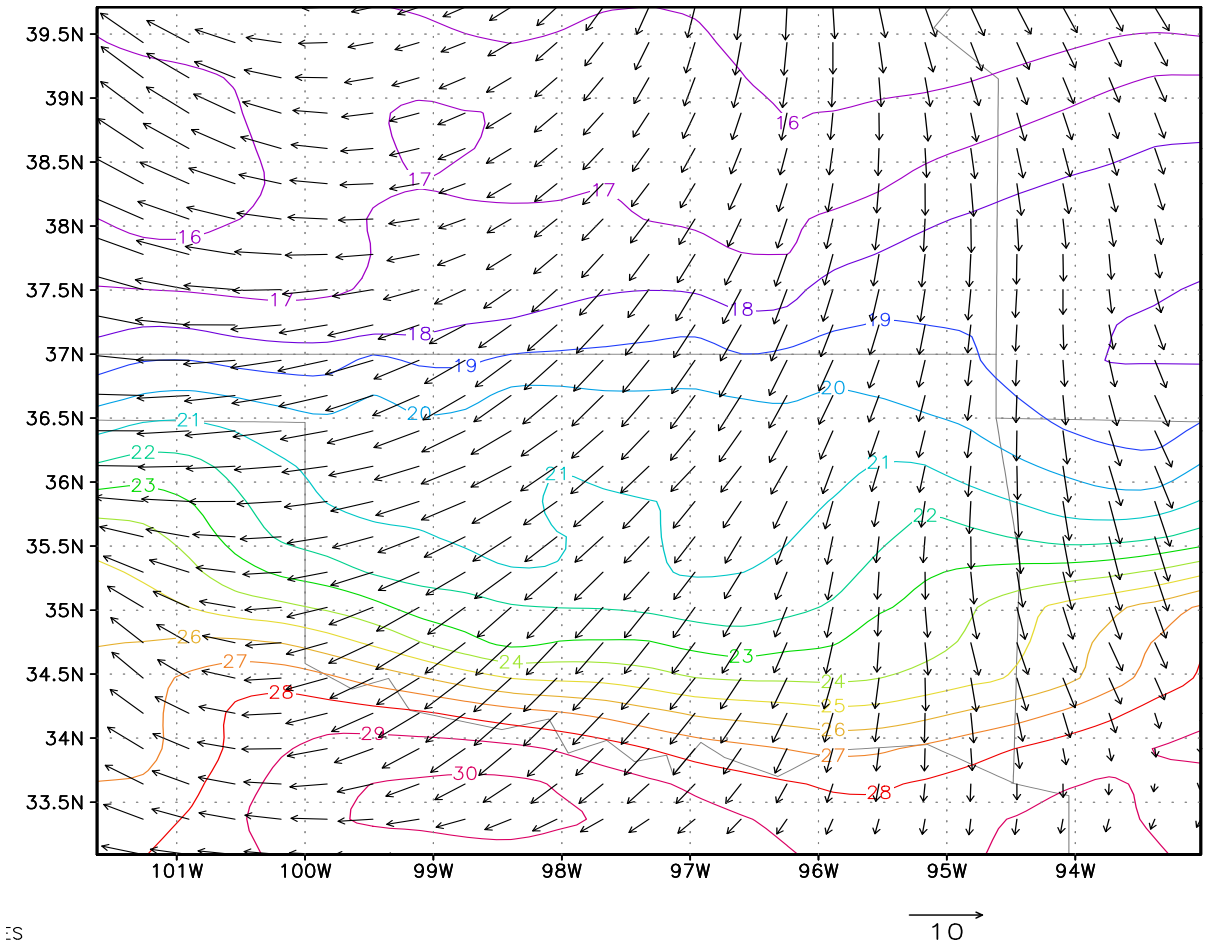
39.5N
39N
38.5N
38N
37.5N
37N
36.5N
36N
35.5N
35N
34.5N
34N
33.5N
101W
100W
99W
98W
97W
96W
95W
94W
10

c

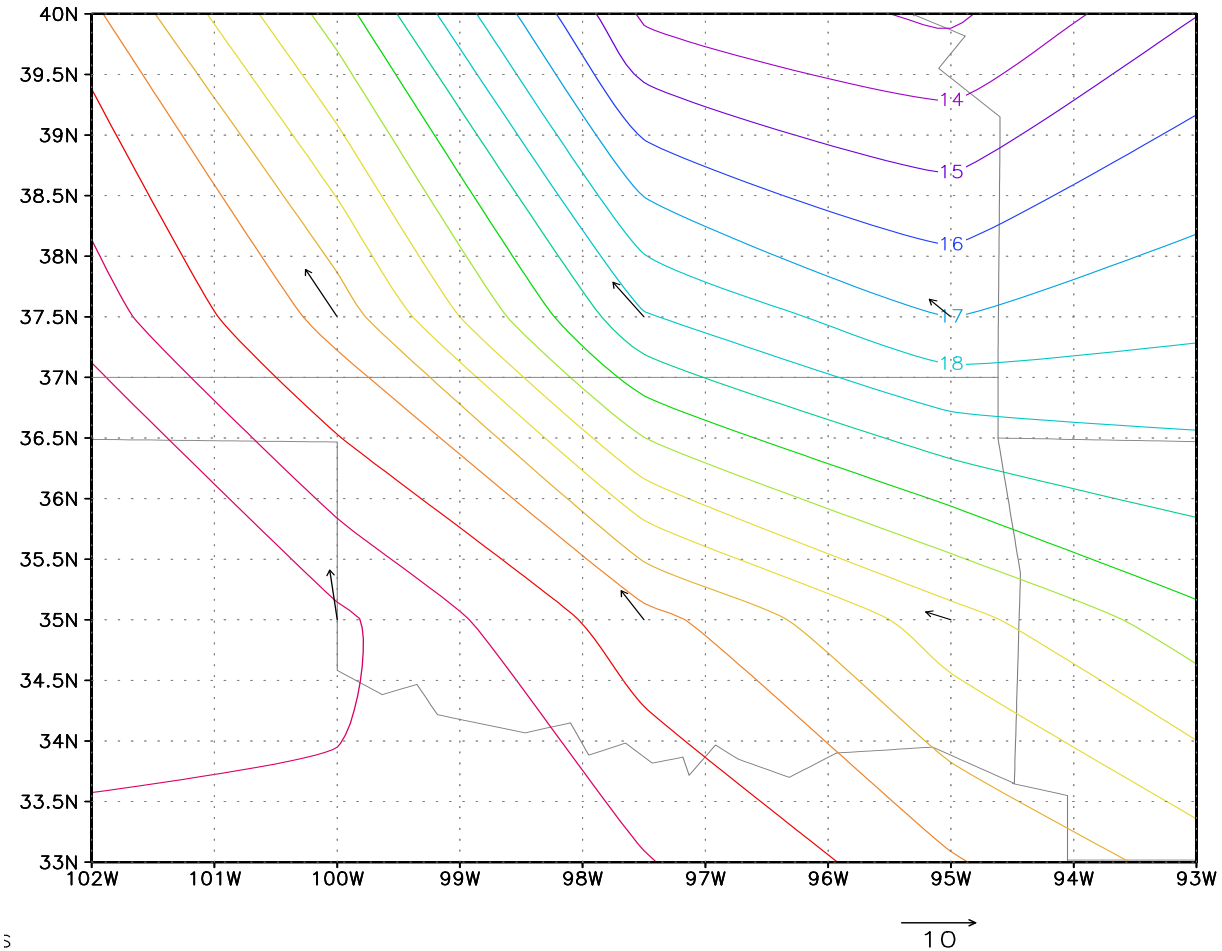
40N
39.5N
39N
38.5N
38N
37.5N
37N
36.5N
36N
35.5N
35N
34.5N
34N
33.5N
33N
102W
101W
100W
99W
98W
97W
96W
95W
94W
93W
14
15
16
17
18
10

d

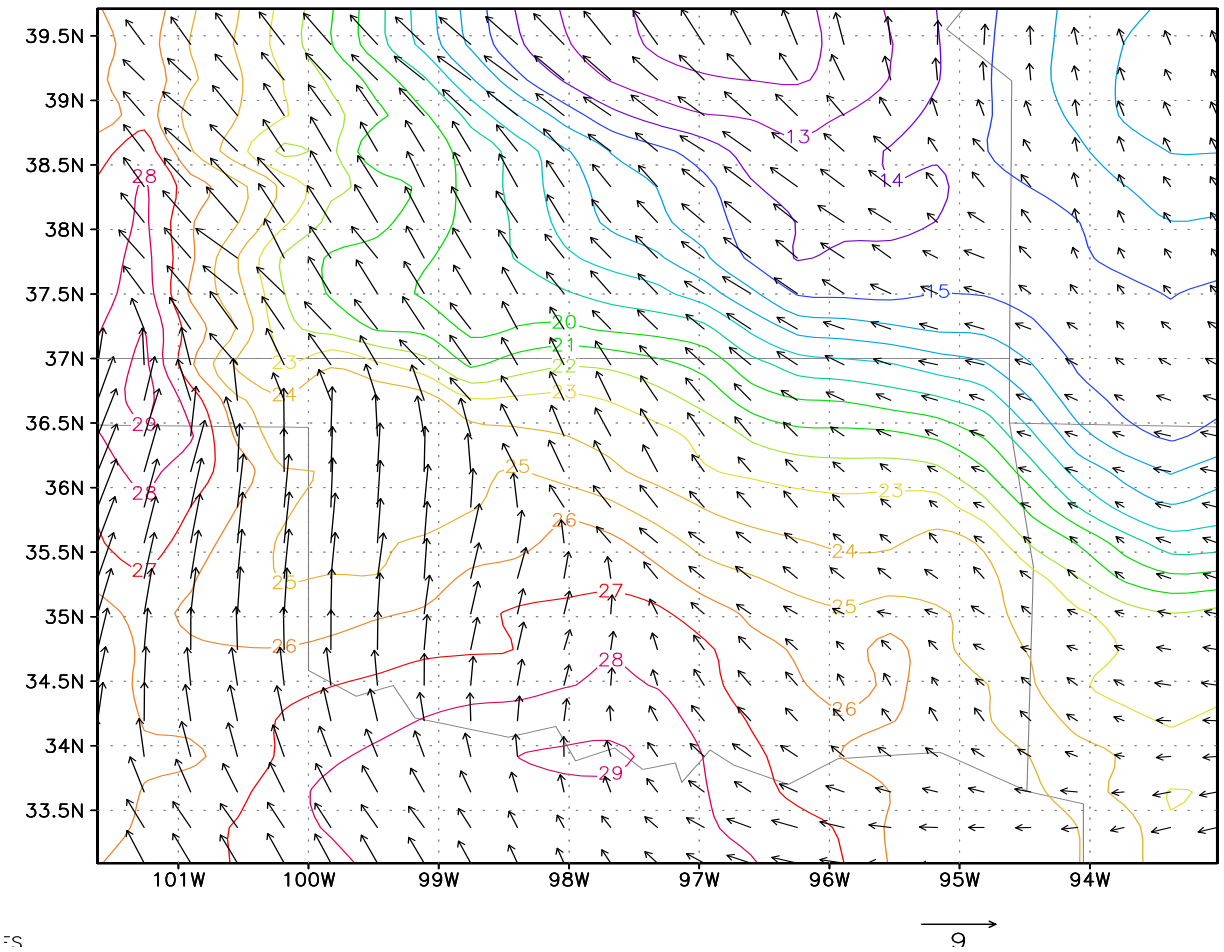
39.5N
39N
38.5N
38N
37.5N
37N
36.5N
36N
35.5N
35N
34.5N
34N
33.5N
101W
100W
99W
98W
97W
96W
95W
94W
13
14
15
20
21
22
23
24
25
26
27
28
29

e

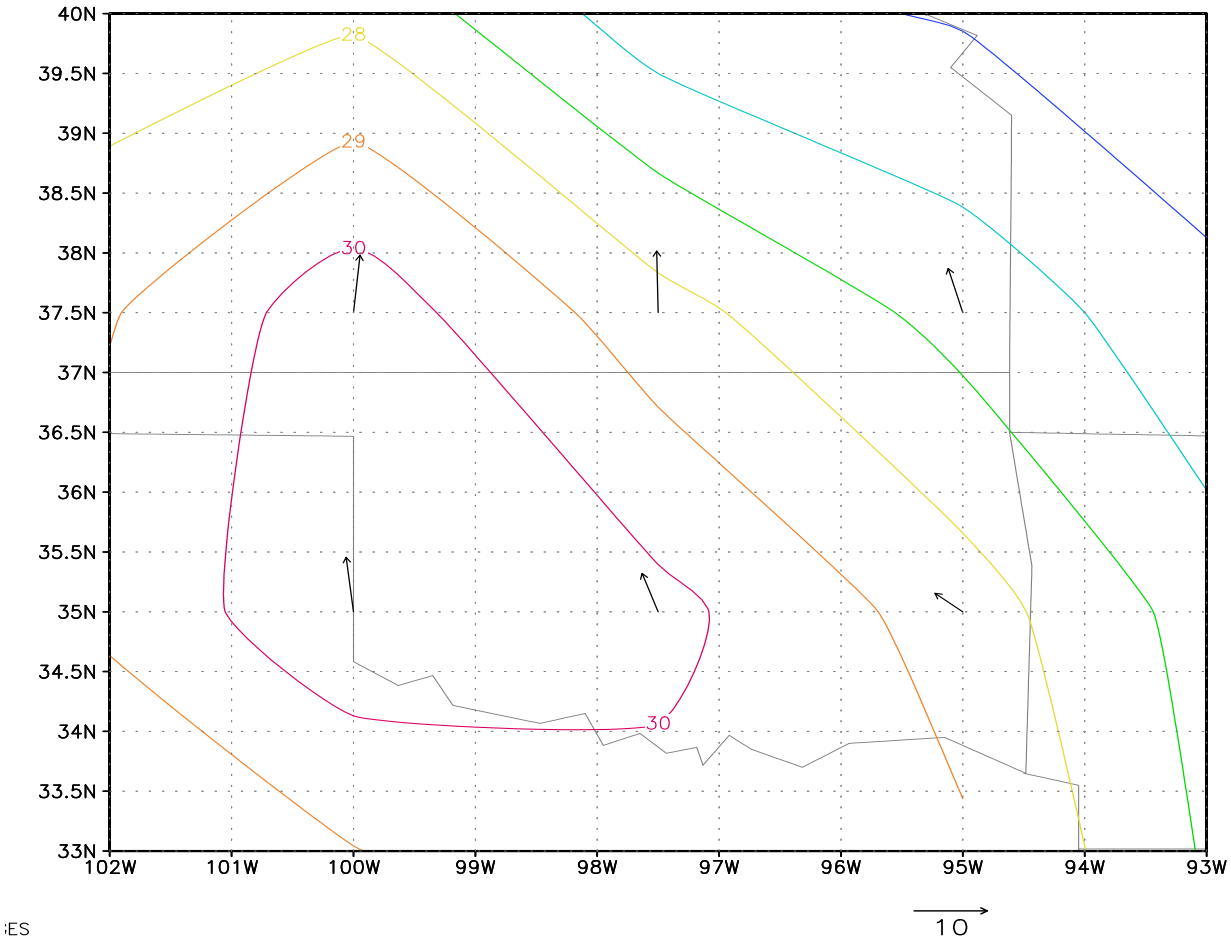
40N
39.5N
39N
38.5N
38N
37.5N
37N
36.5N
36N
35.5N
35N
34.5N
34N
33.5N
33N
102W
101W
100W
99W
98W
97W
96W
95W
94W
93W
28
29
30
30
10

f

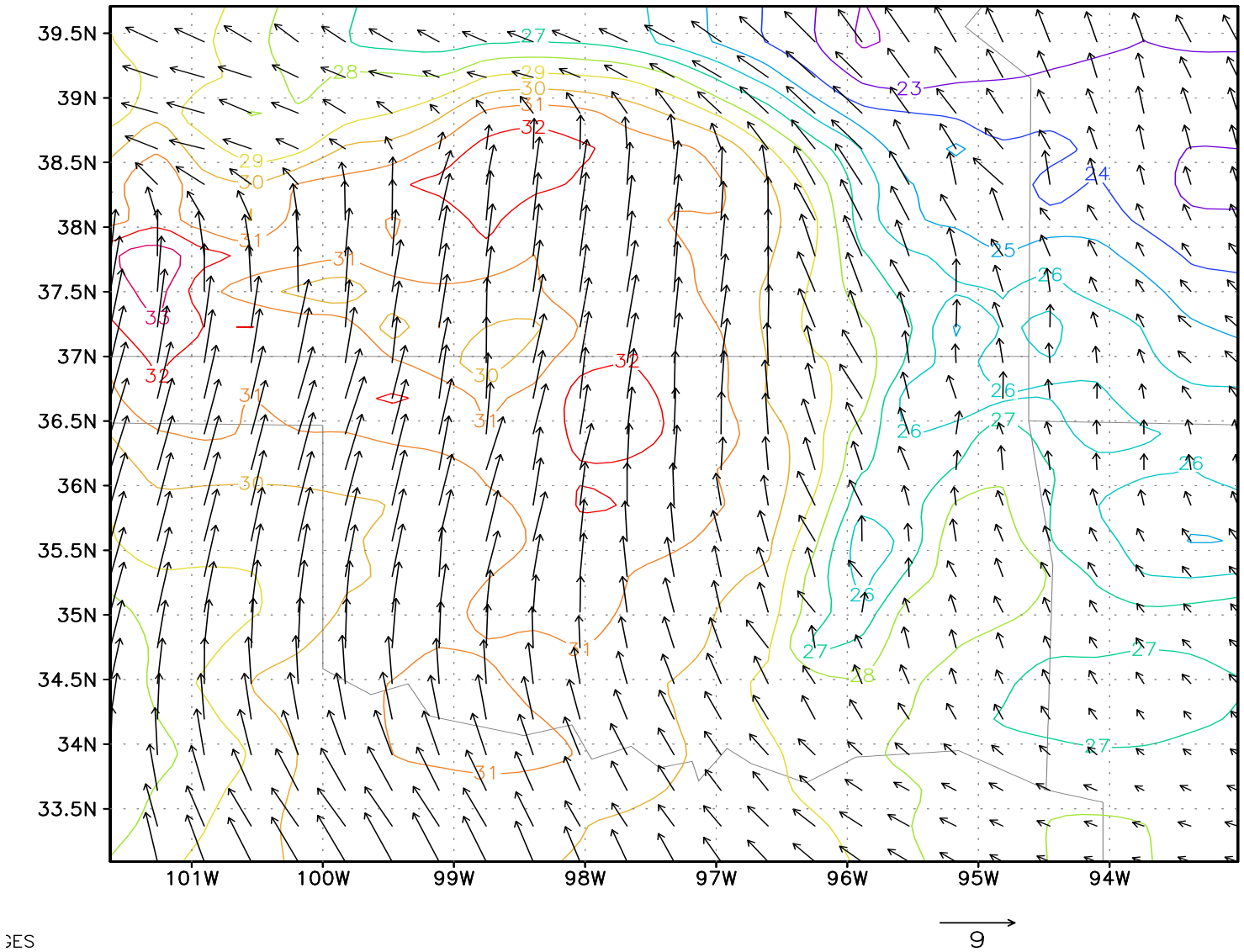
39.5N
39N
38.5N
38N
37.5N
37N
36.5N
36N
35.5N
35N
34.5N
34N
33.5N
101W
100W
99W
98W
97W
96W
95W
94W
9

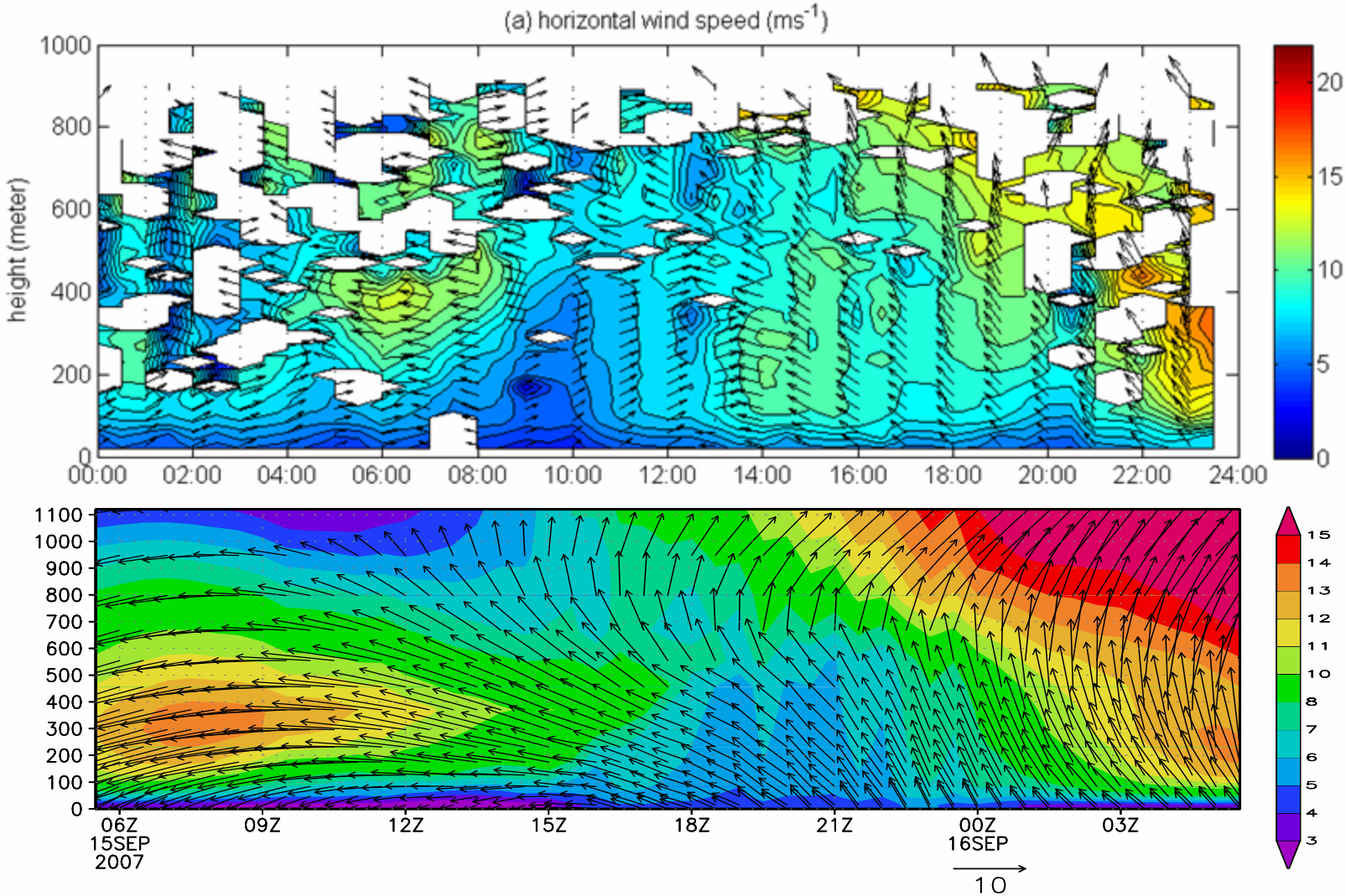

Figure 4 SODAR (top) vs. RAMS (bottom) 9/15 (midnight to midnight) wind speed (m/s, colors) and direction (arrows).

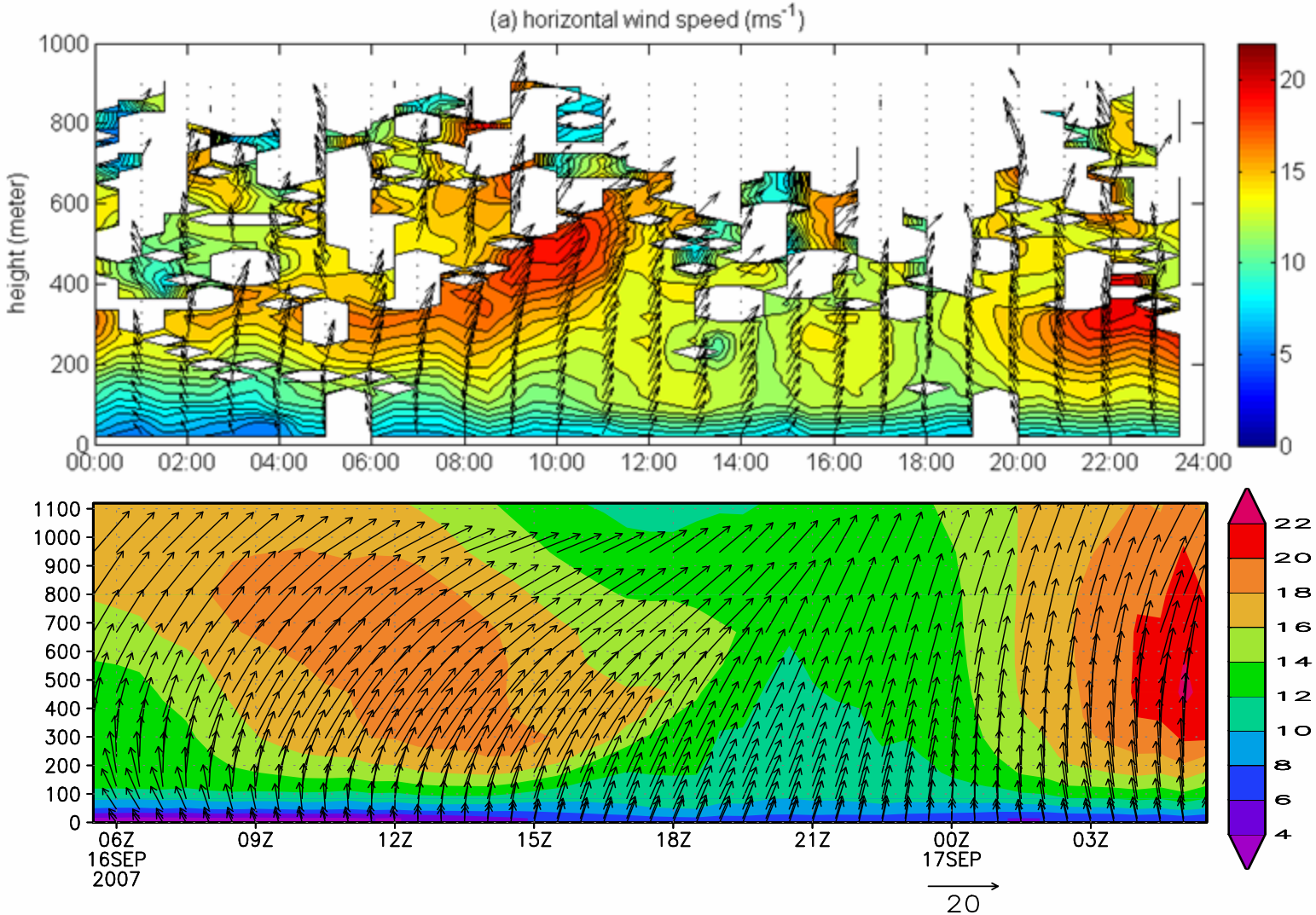

Figure 5 As in Fig. 3 but for 9/16.

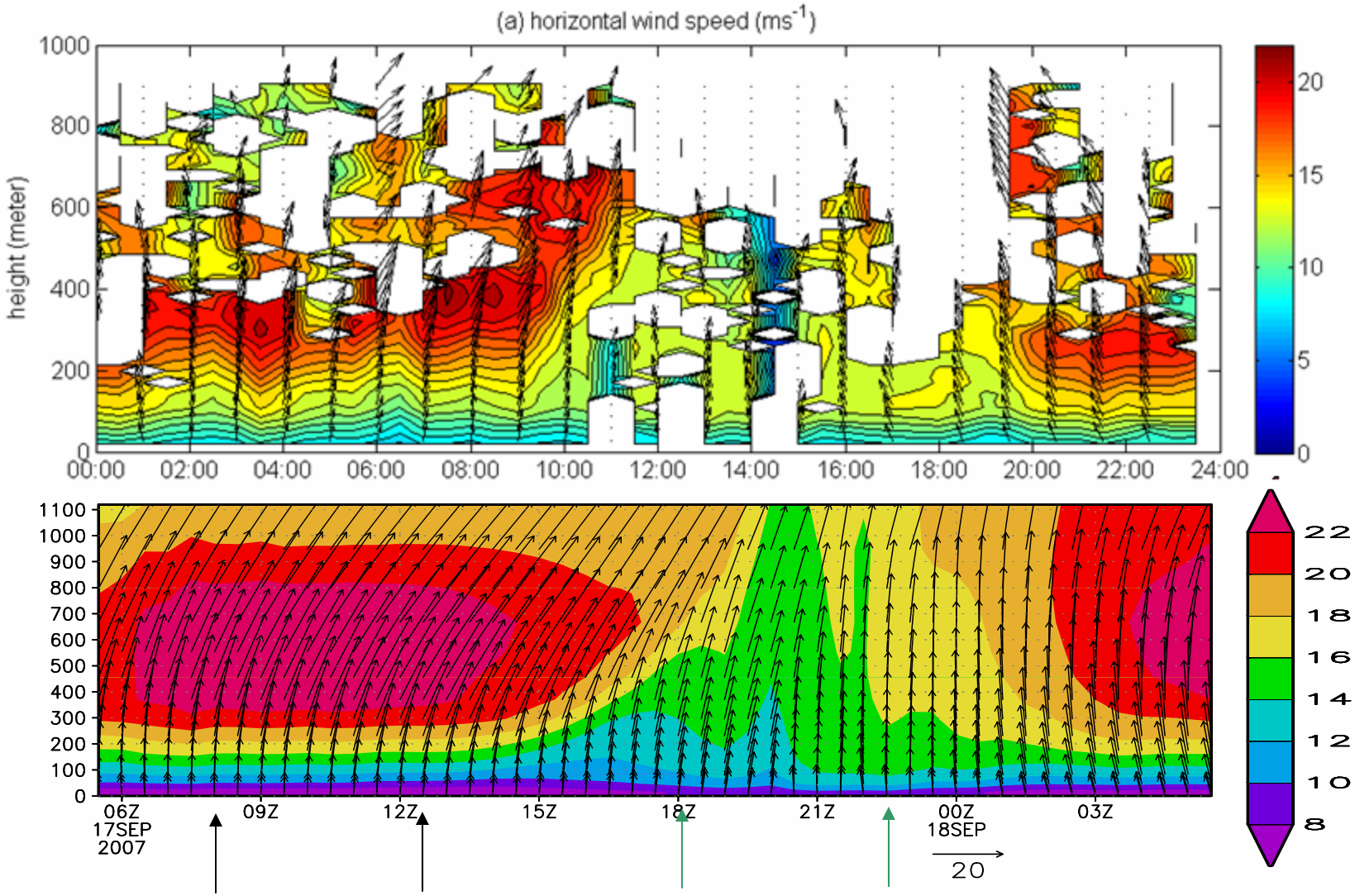

Figure 6 As in Fig. 4 but for 9/17. The black arrows indicate the nocturnal period simulated by the high-resolution model, and the green arrows indicate the daytime high-resolution simulation.

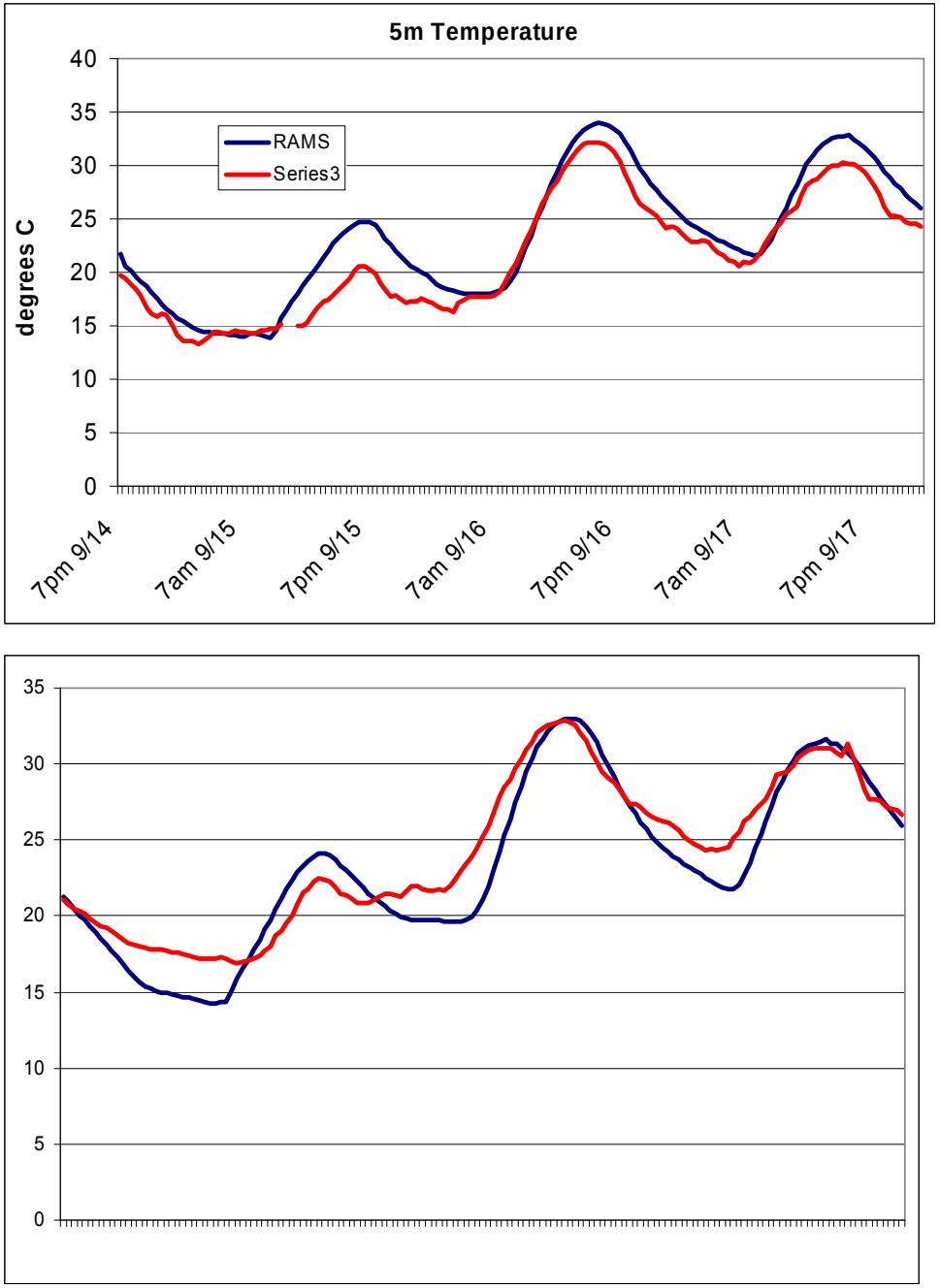

Fig. 7 Temperature (ºC) at the tower (red) and in the model (blue) at (top) 5m and (bottom) 60m at the ARM site.

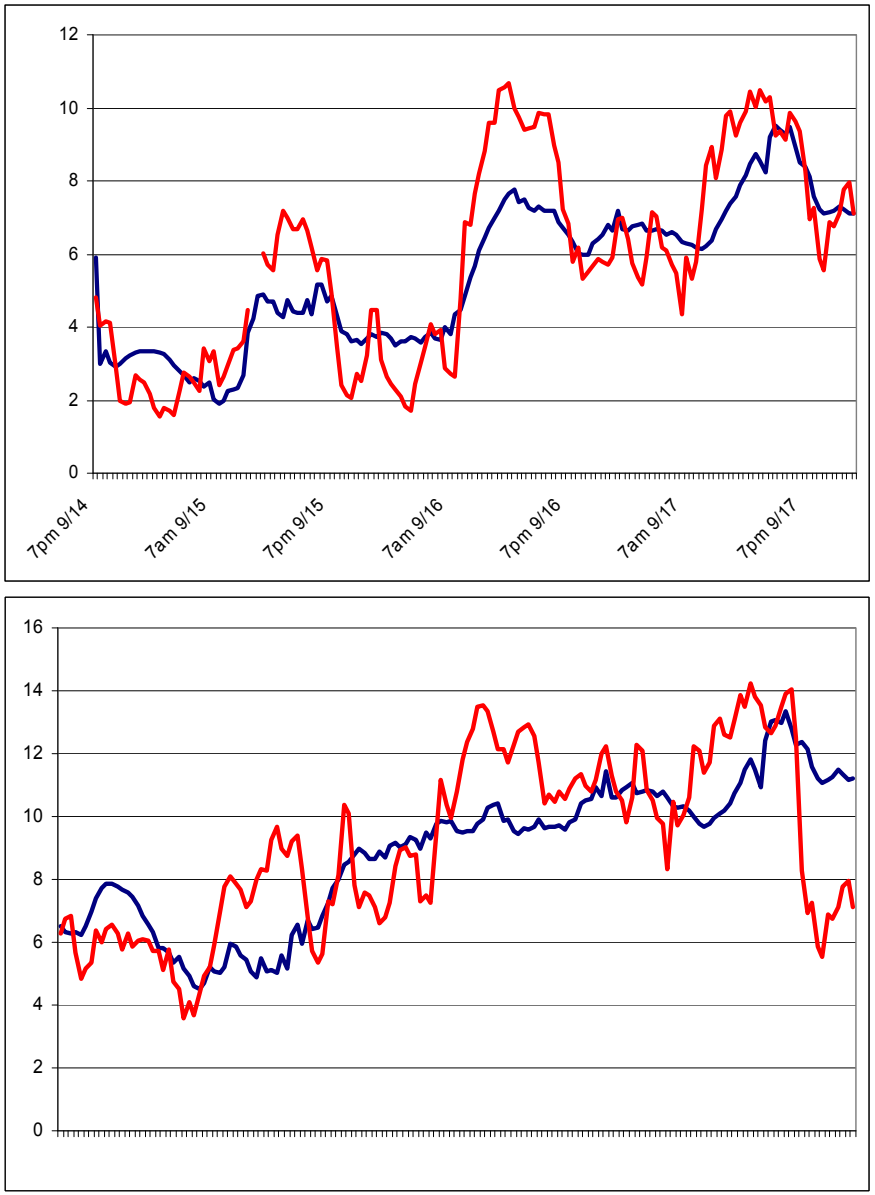

Fig. 8 As in Fig. 7 but for wind speed.

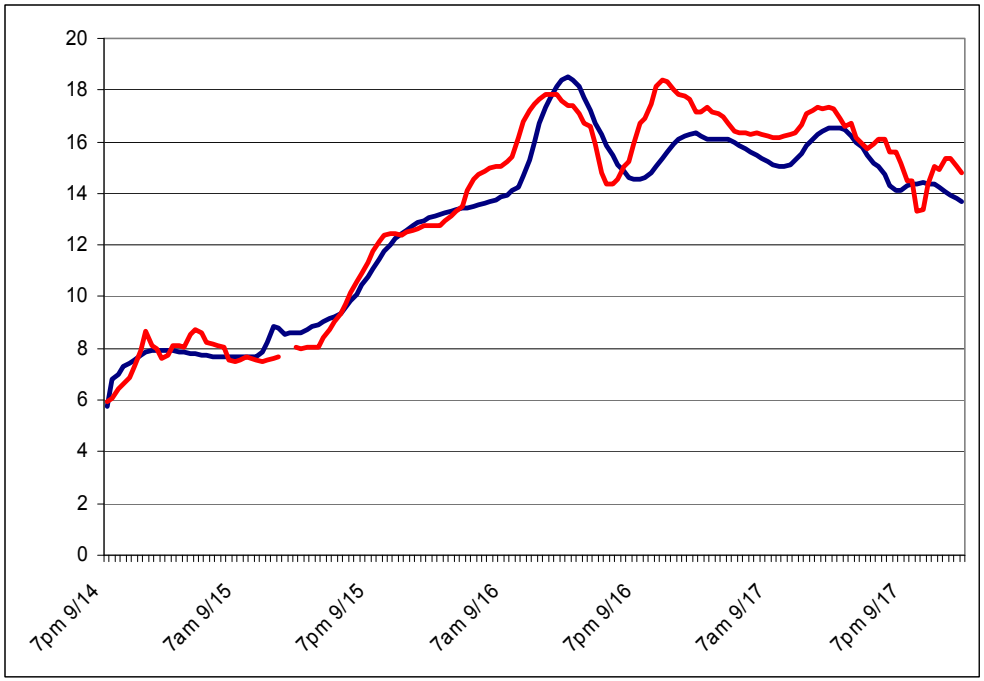

Fig. 9 Water vapor (g/m^3) at the tower (red) and in the model (blue) at 5m at the ARM site.

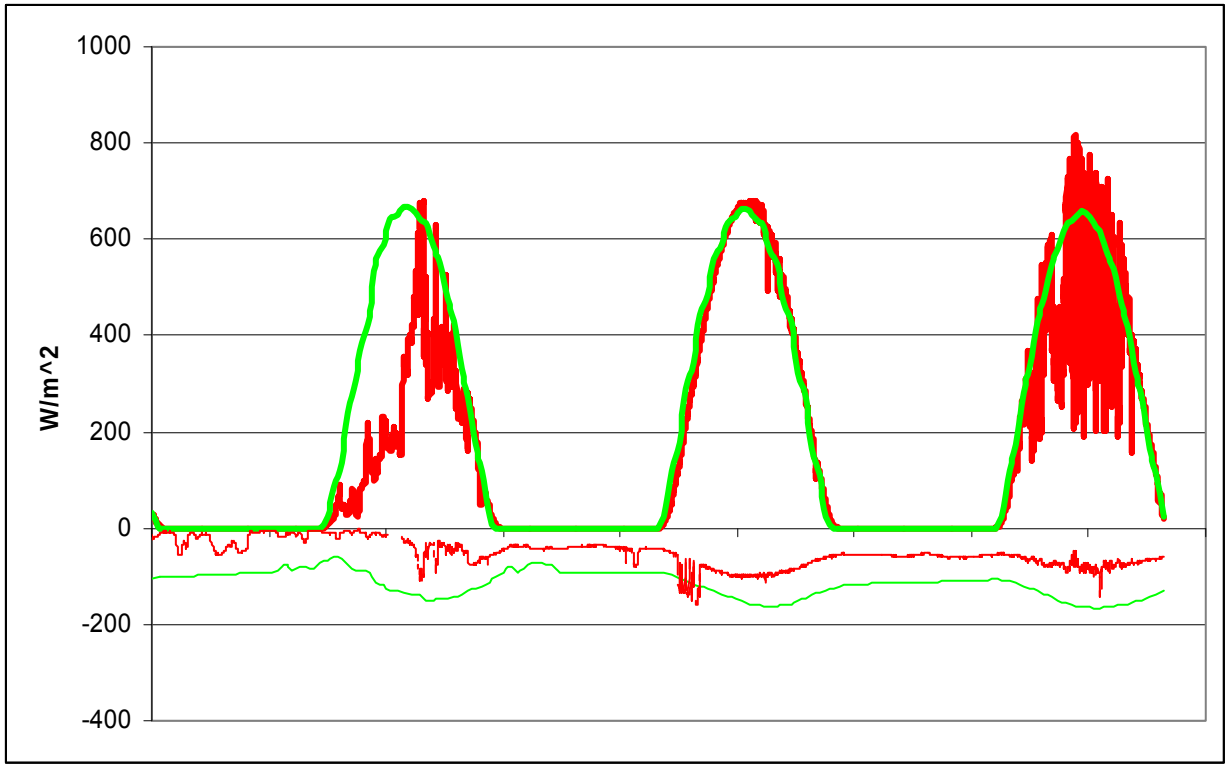

Fig. 10 Modeled (green) and observed (red) values of net shortwave (thick line) and net longwave (thin line).

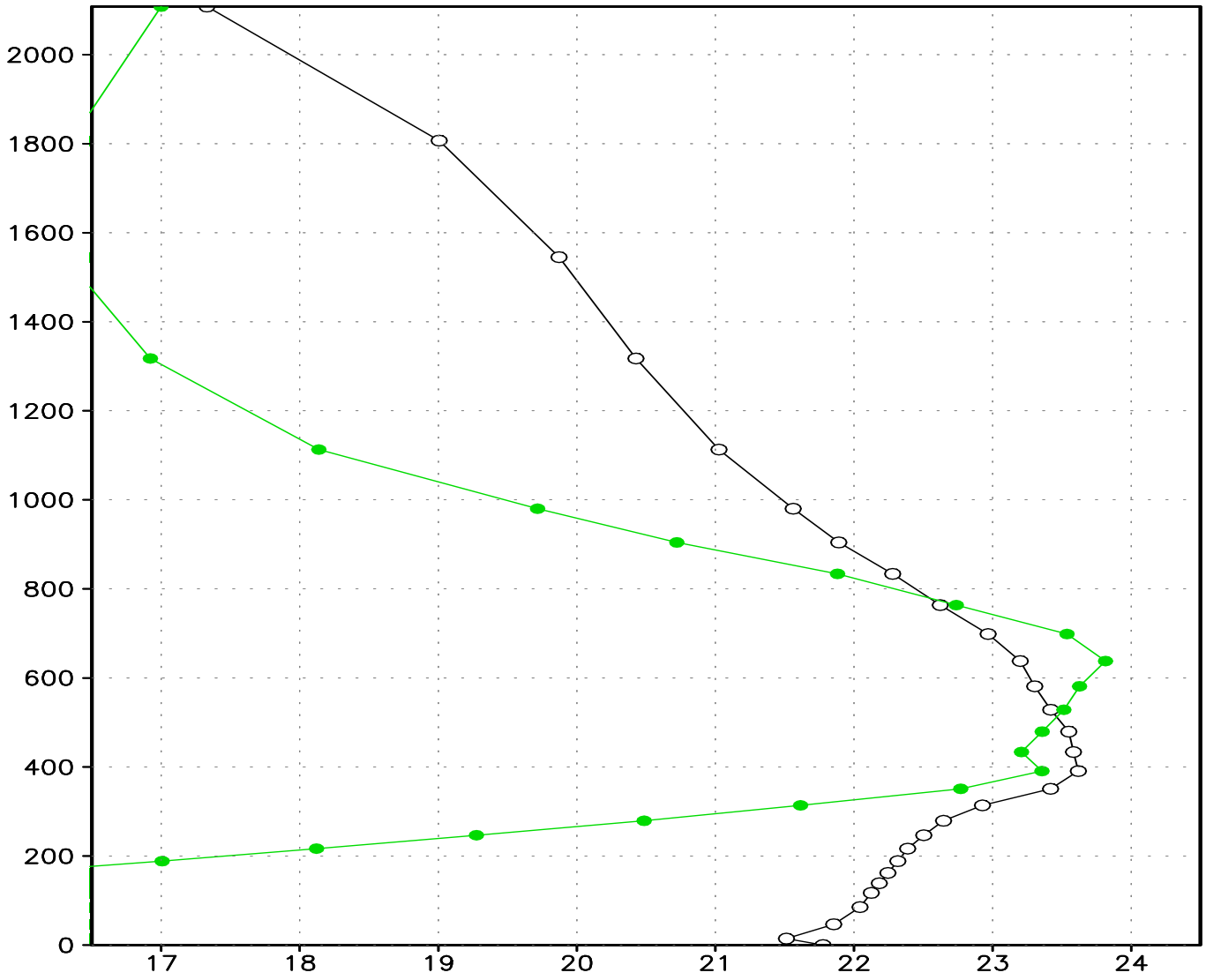

Fig. 11 Sounding of model temperature (black) and wind speed (green) at 10Z, Sept. 17.

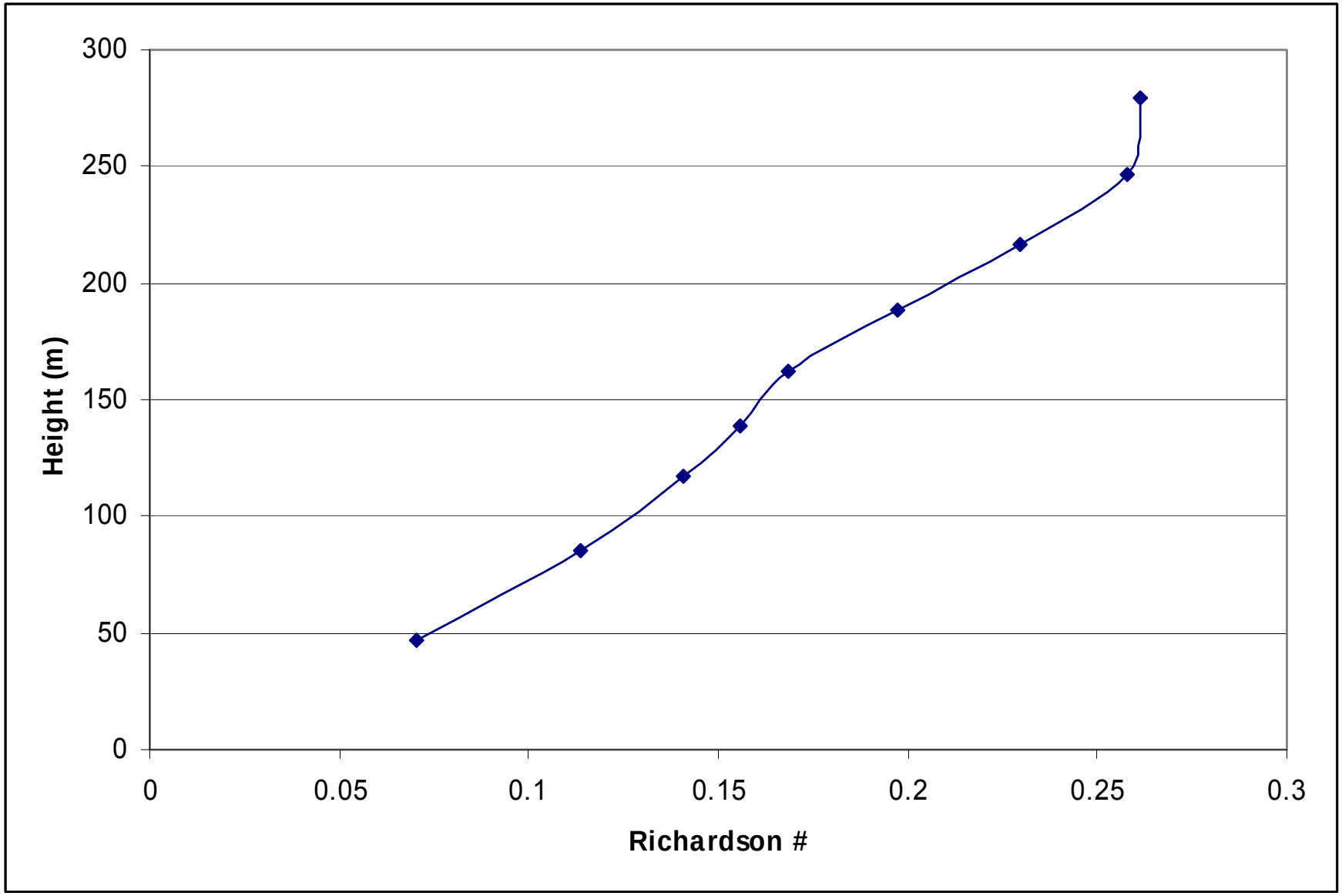

Fig. 12 Model Richardson number averaged over the 4.5 hour simulation period.

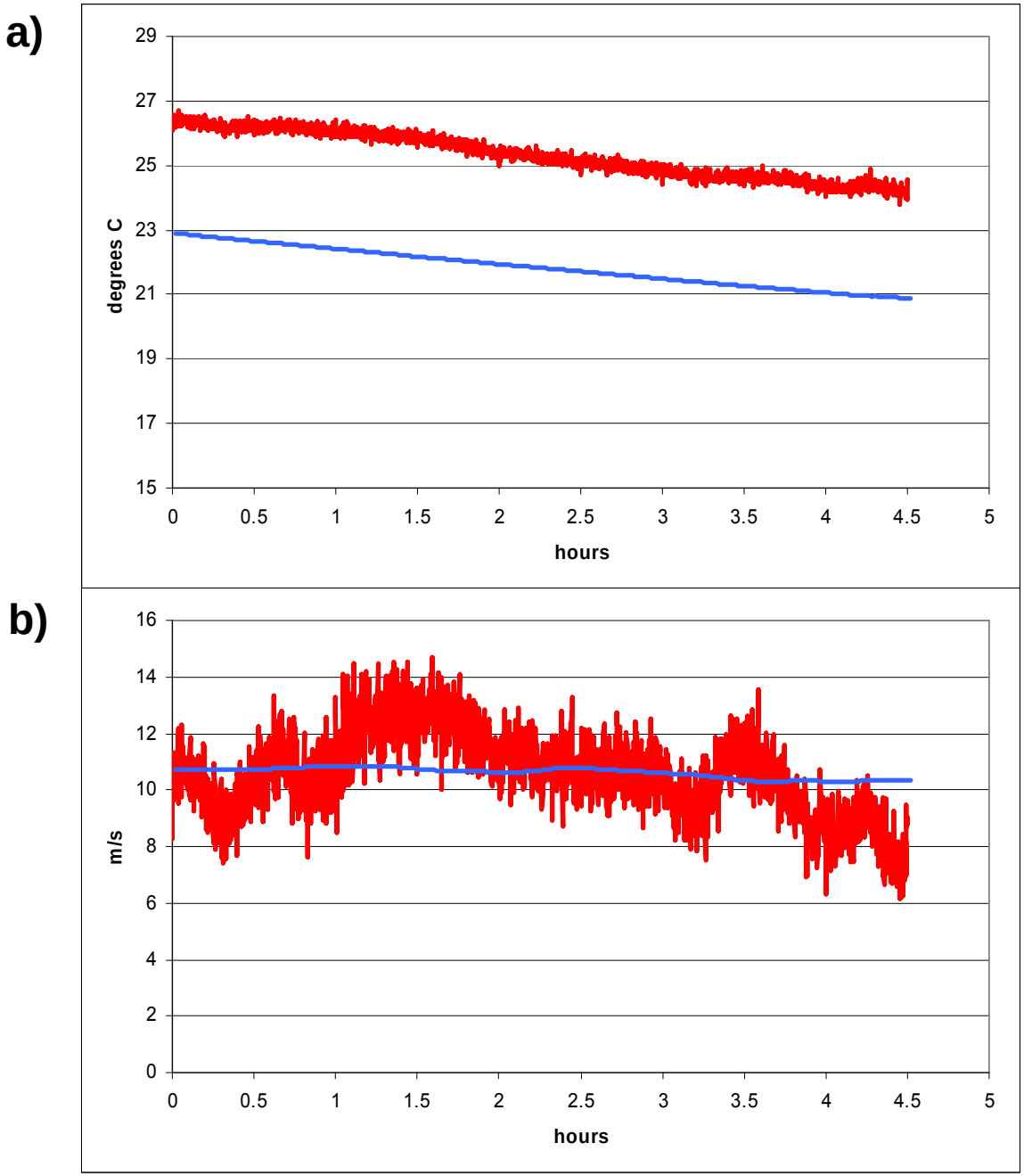

Figure 13 Observed (red) and simulated (blue) 60m a) temperature and b) wind speed of the nocturnal 4.5 hour high resolution run.

a)

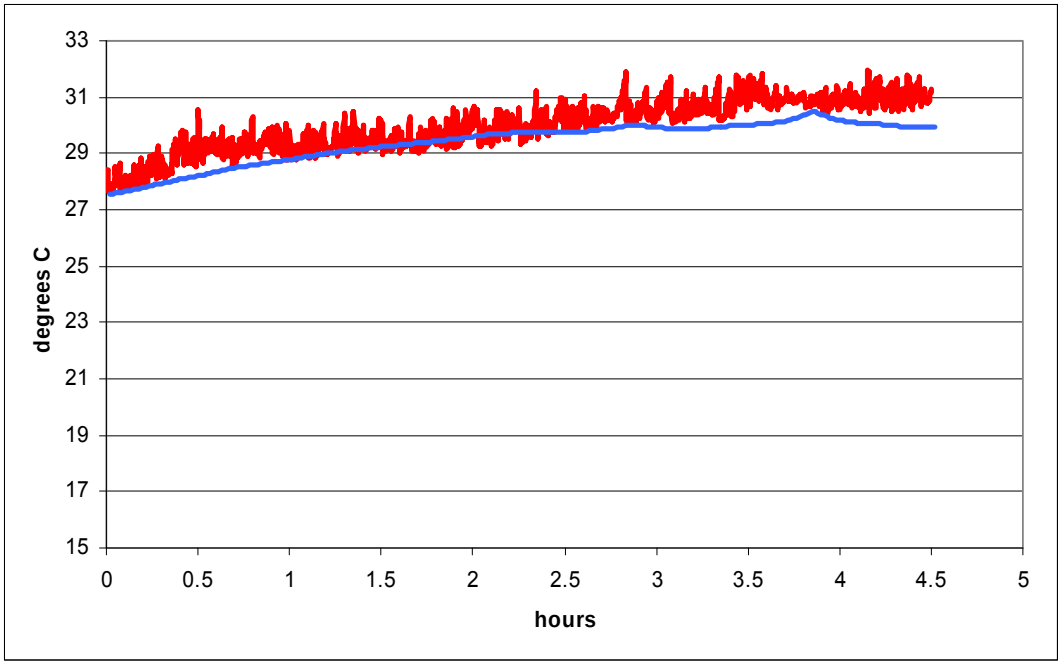

b)

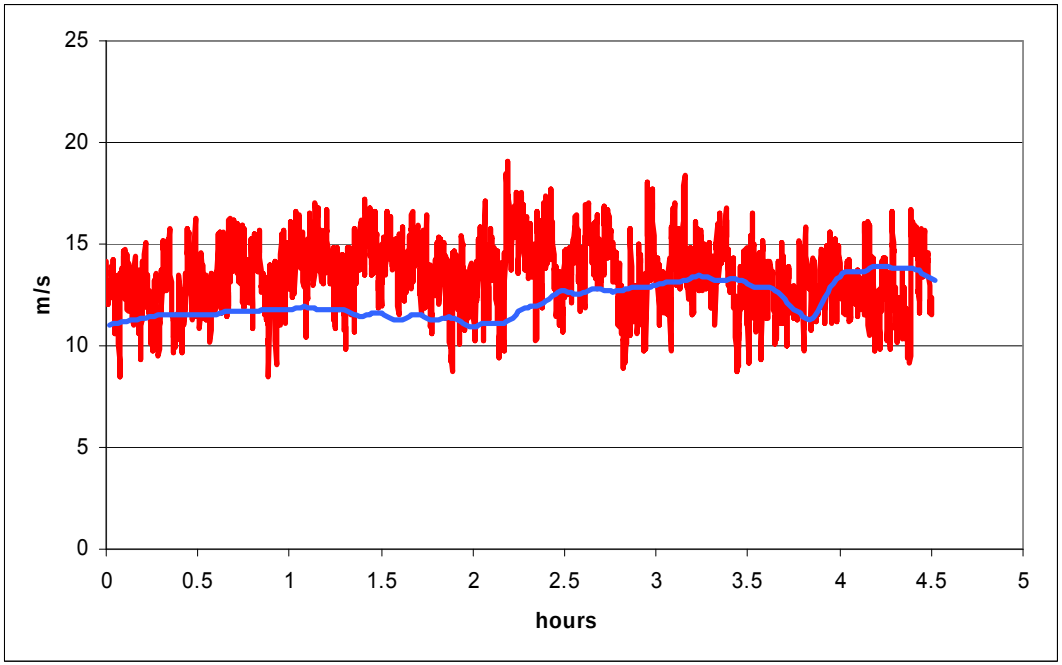

Fig. 14 As in Fig. 13 but for the daytime run.

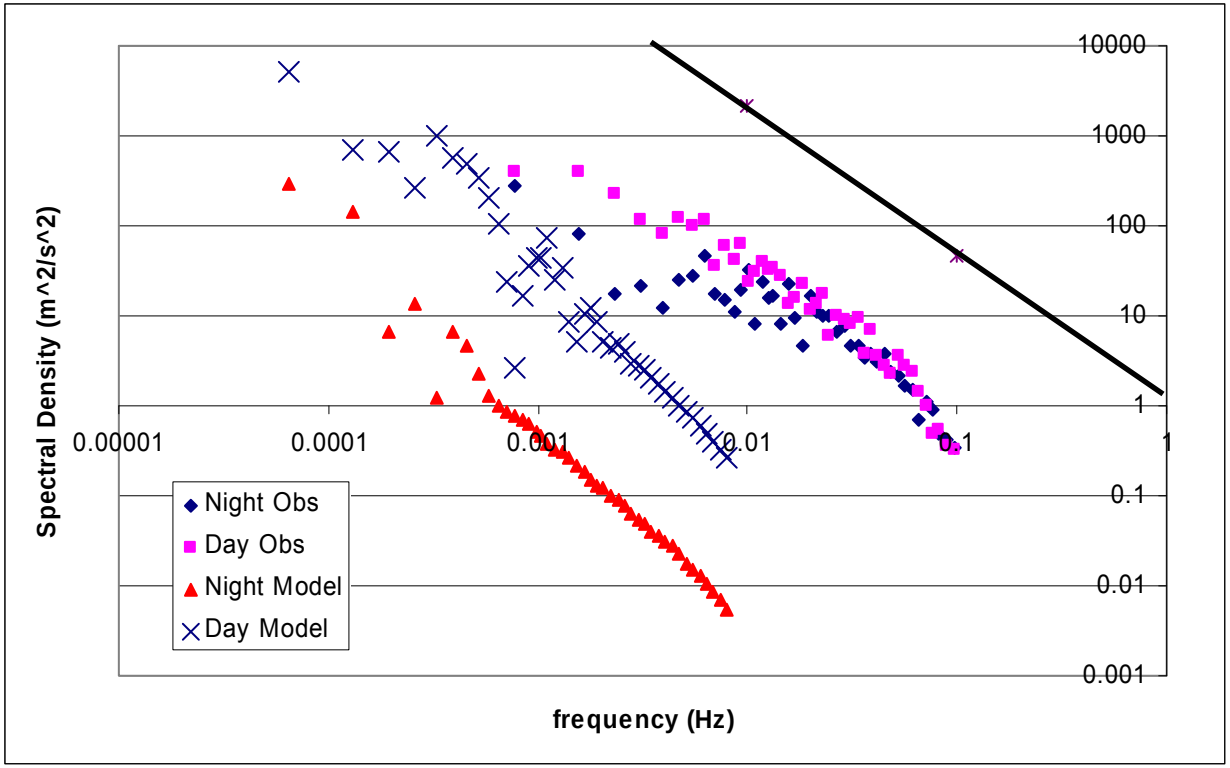

Fig. 15 Power spectra of the 60m windspeed. The black line follows a -5/3 power law.

a)

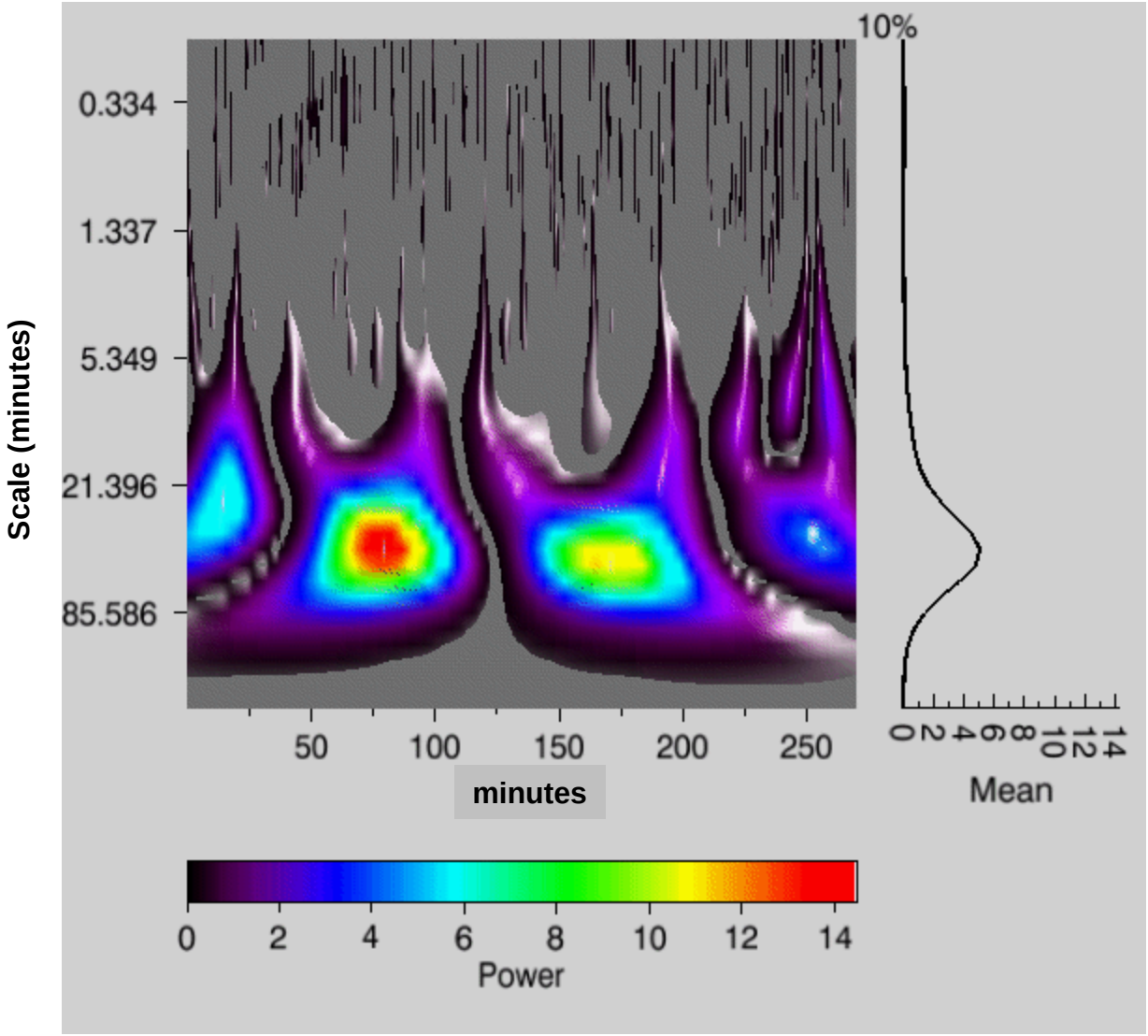

Fig. 16 Wavelet analysis of a) Observed 60m temperature, Sept. 17, 2007, 8Z-1230Z

b)

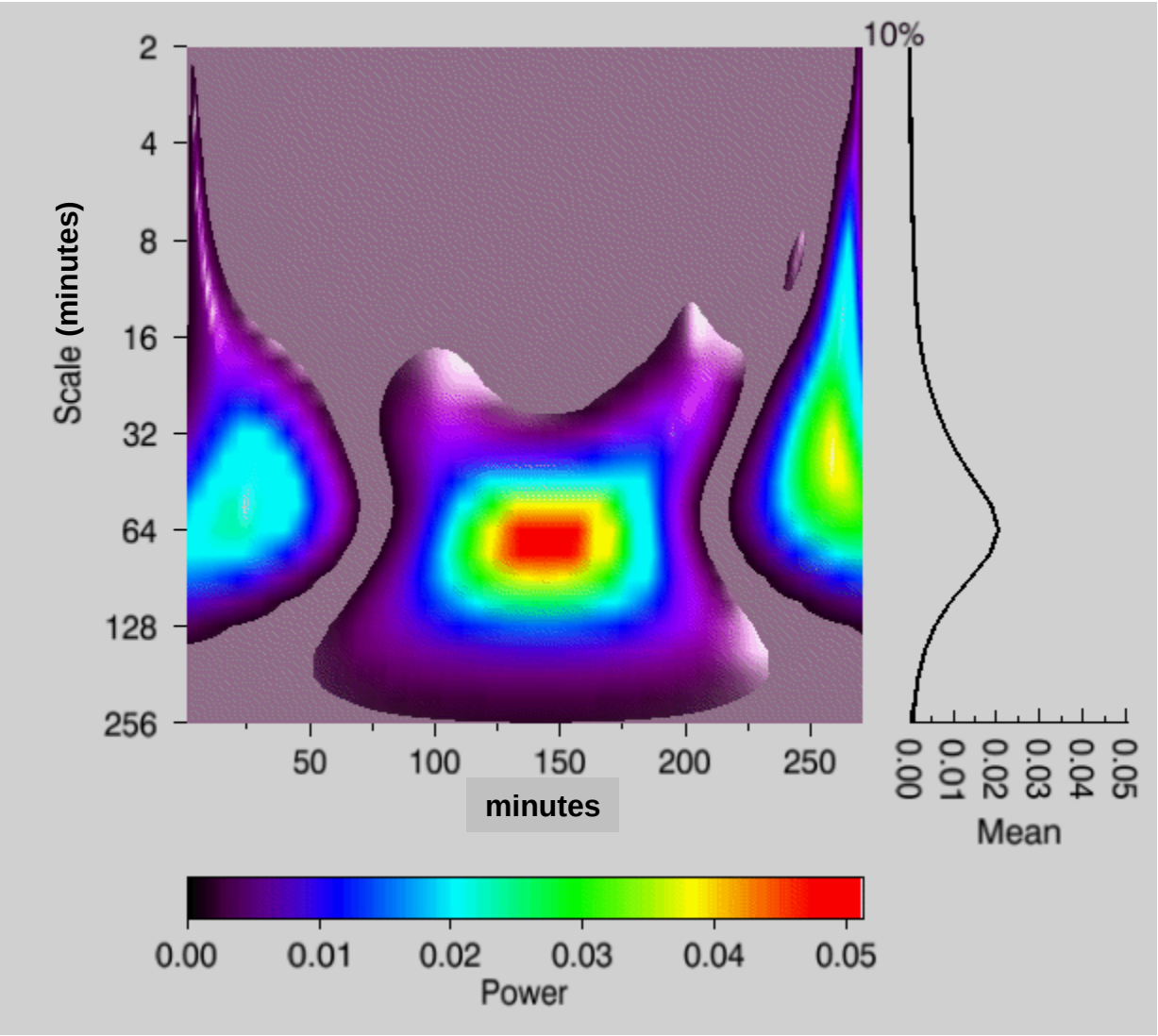

Fig. 16 b) As in a) but for the model temperature.

c)

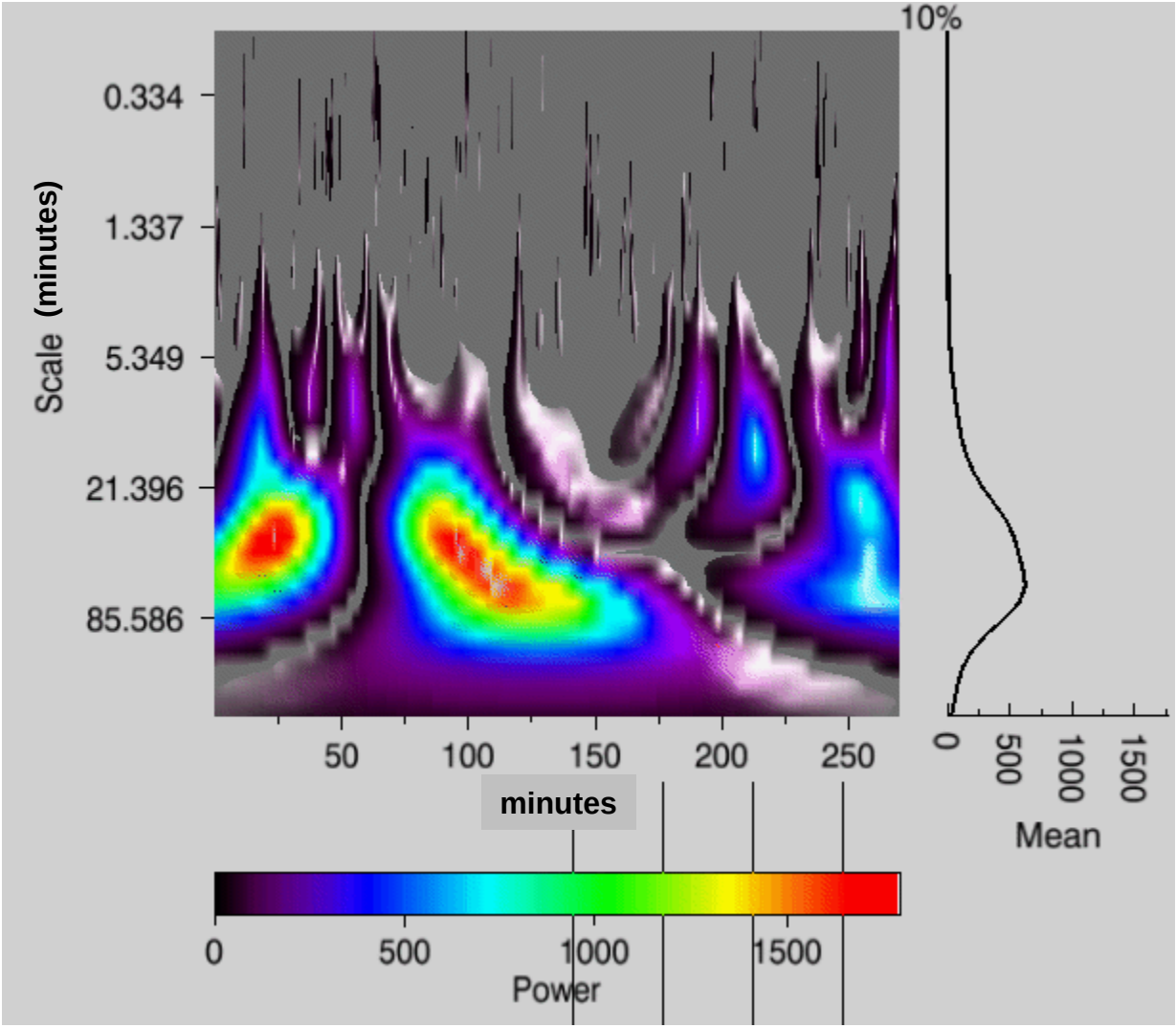

Fig. 16 c) As in a) but for the observed windspeed.

d)

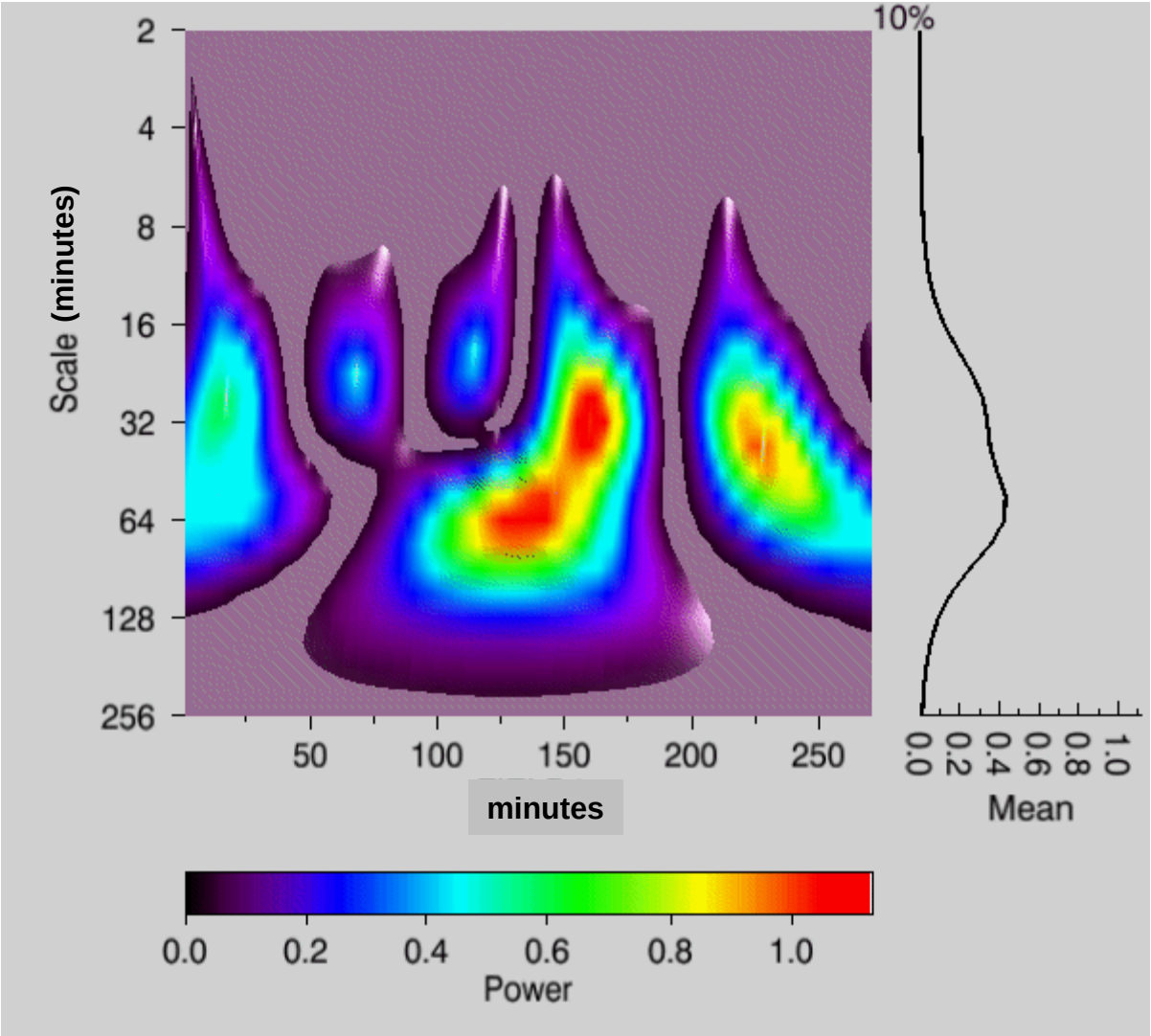

Fig. 16 d) As in b) but for the model windspeed.

a)

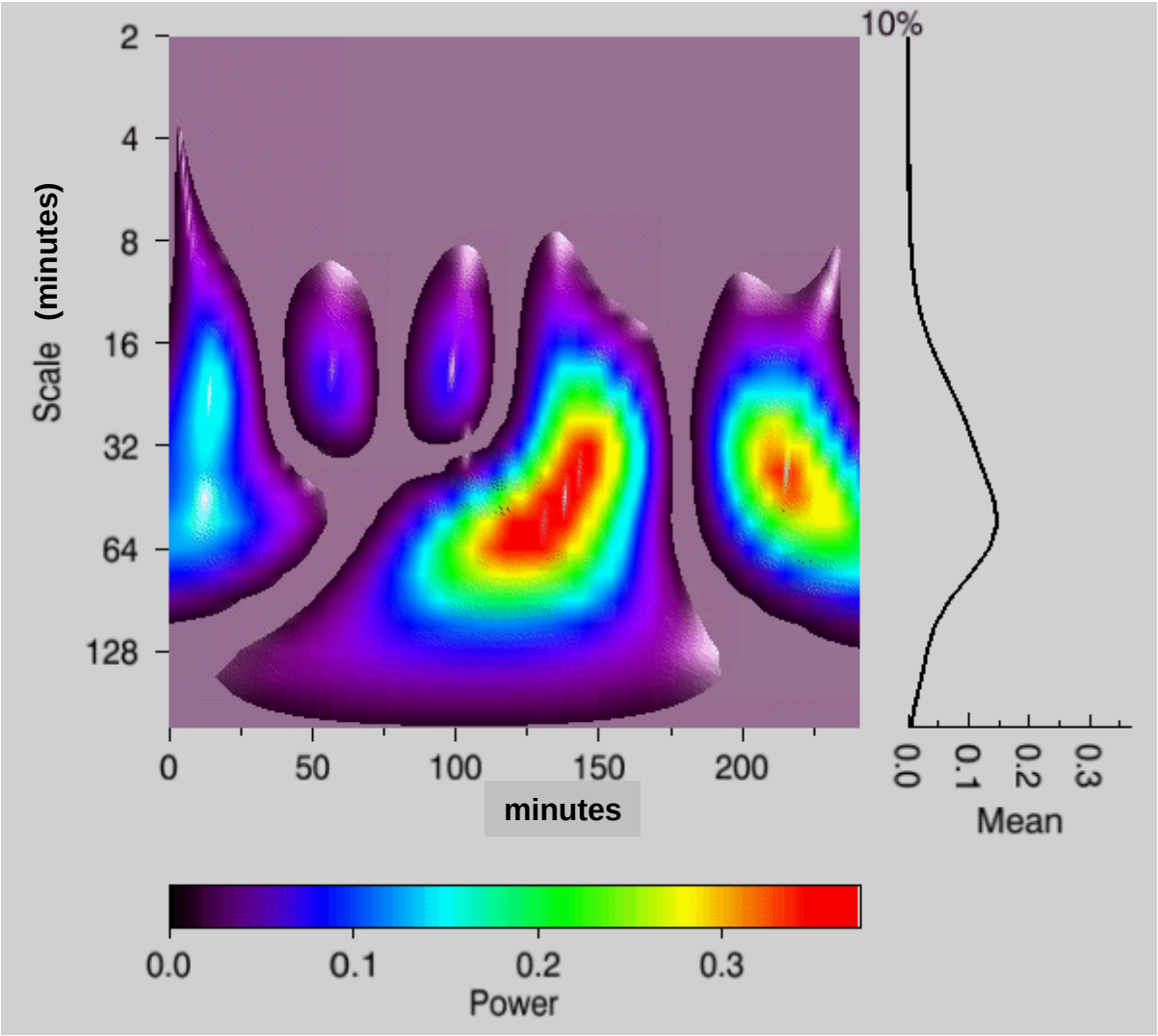

Fig. 17 Wavelet analysis of the low frequency model windspeed at a) the surface, b) 164m, c) 279m, and d) 904m.

b)

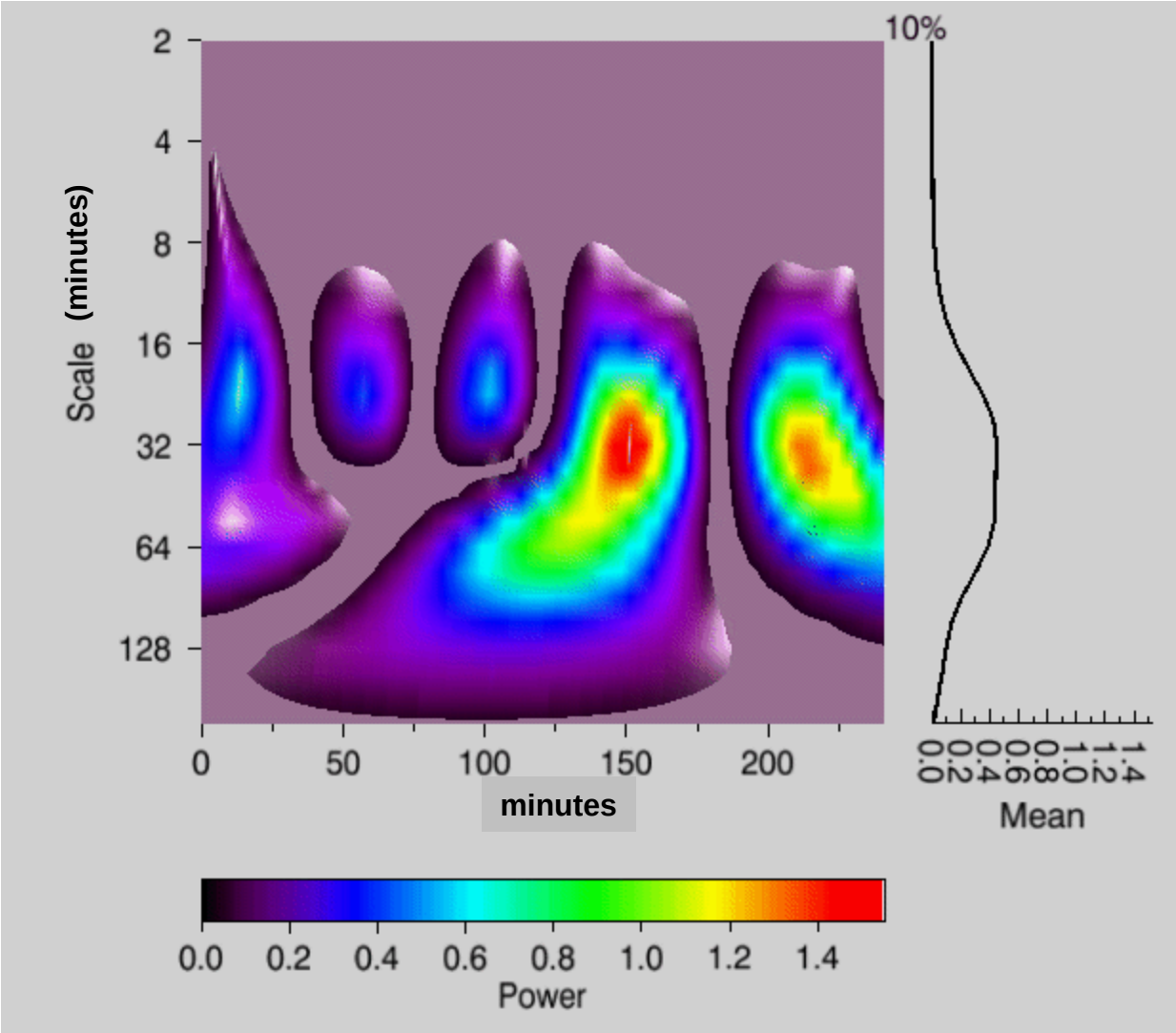
10%
Scale (minutes)
2
4
8
16
32
64
128
0
50
100
150
200
minutes
0.0
0.2
0.4
0.6
0.8
1.0
1.2
1.4
Mean
0.0
0.2
0.4
0.6
0.8
1.0
1.2
1.4
Power

c)

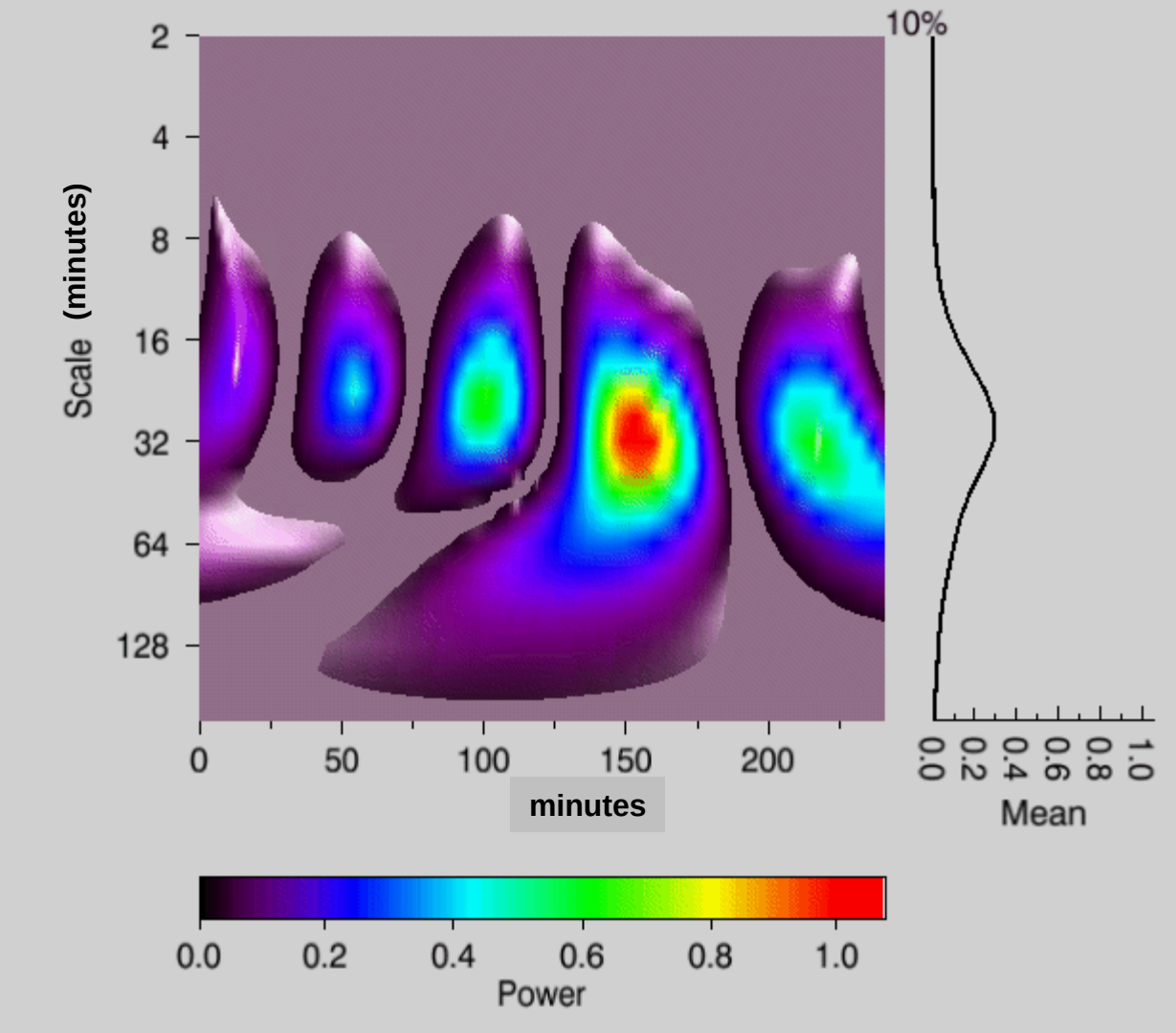
Scale (minutes)
2
4
8
16
32
64
128
0
50
100
150
200
minutes
10%
0.0
0.2
0.4
0.6
0.8
1.0
Mean
0.0
0.2
0.4
0.6
0.8
1.0
Power

d)

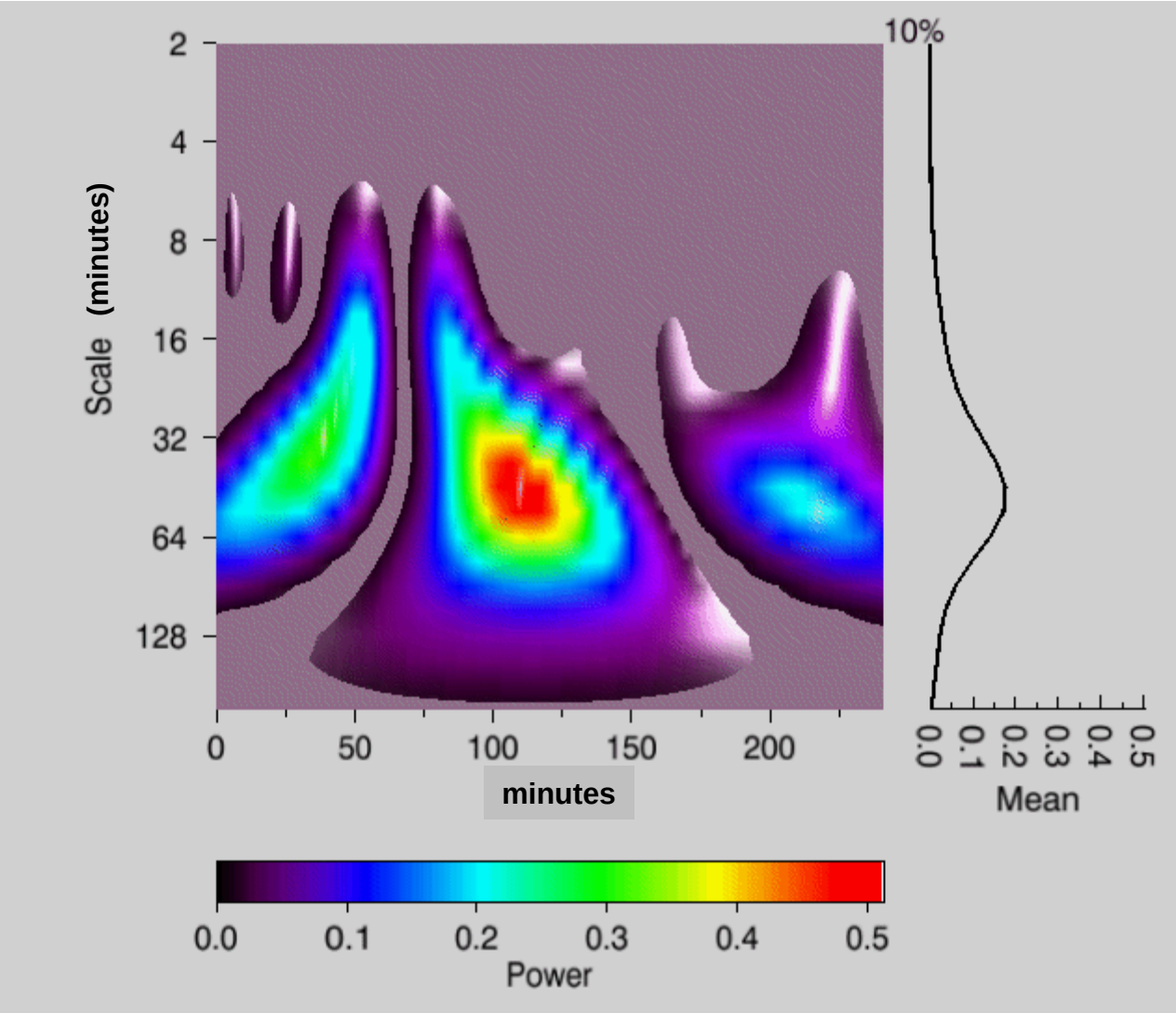
10%
Scale (minutes)
2
4
8
16
32
64
128
0
50
100
150
200
minutes
0.0
0.1
0.2
0.3
0.4
0.5
Mean
0.0
0.1
0.2
0.3
0.4
0.5
Power

a)

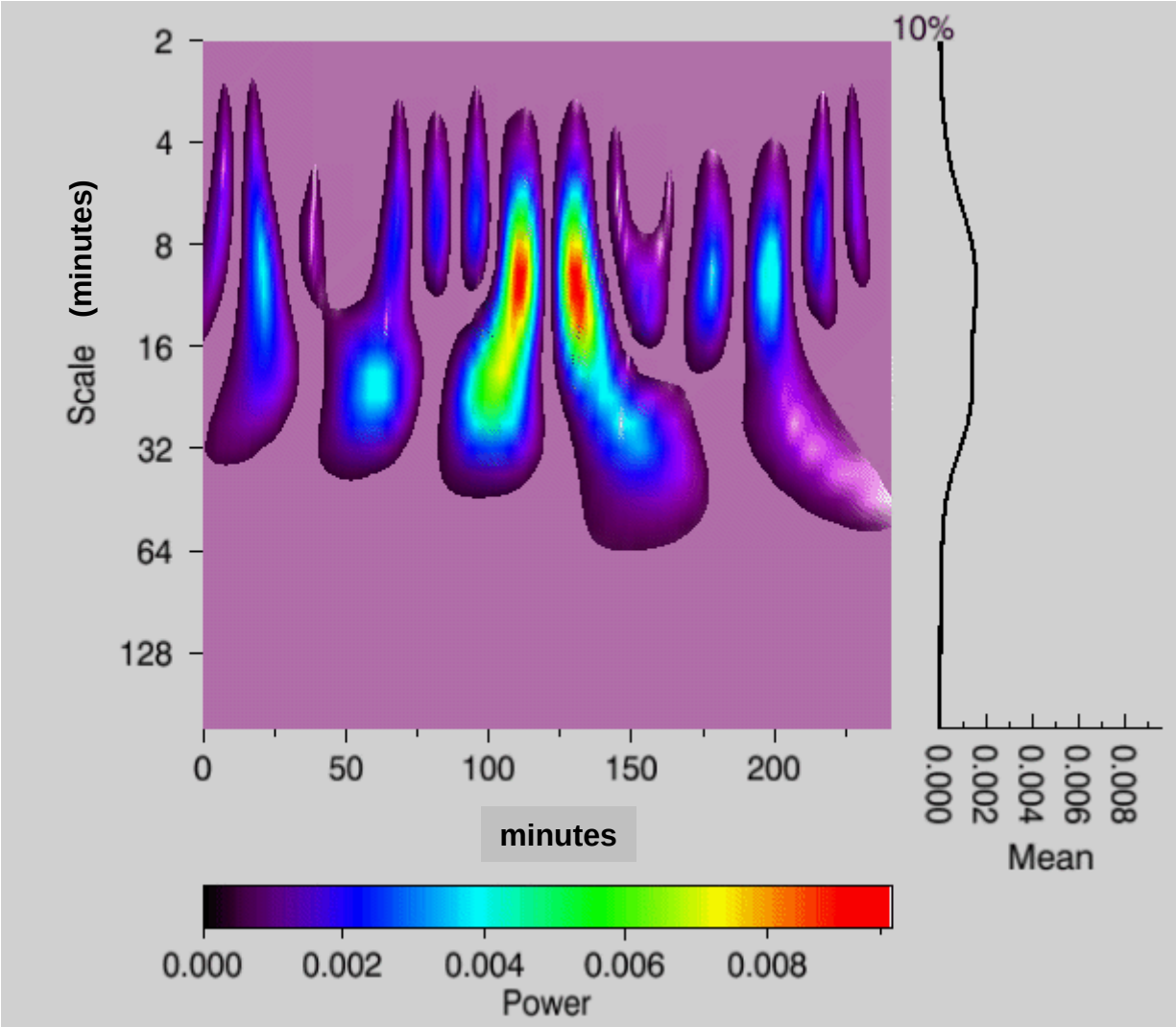

Fig. 18 As in Fig. 17 but for the high frequency component.

b)

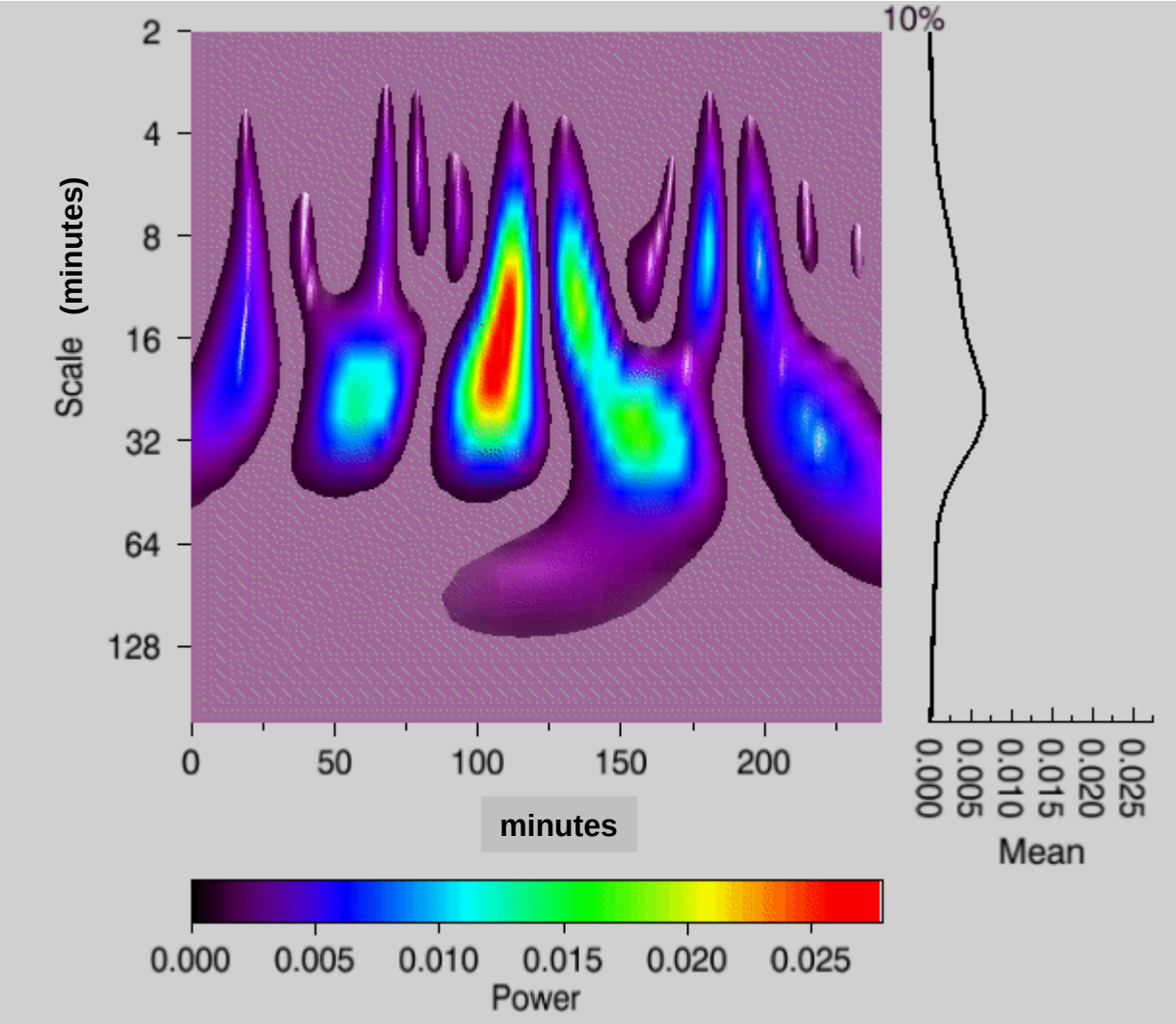
Scale (minutes)
2
4
8
16
32
64
128
0
50
100
150
200
minutes
10%
0.000
0.005
0.010
0.015
0.020
0.025
Mean
0.000
0.005
0.010
0.015
0.020
0.025
Power

c)

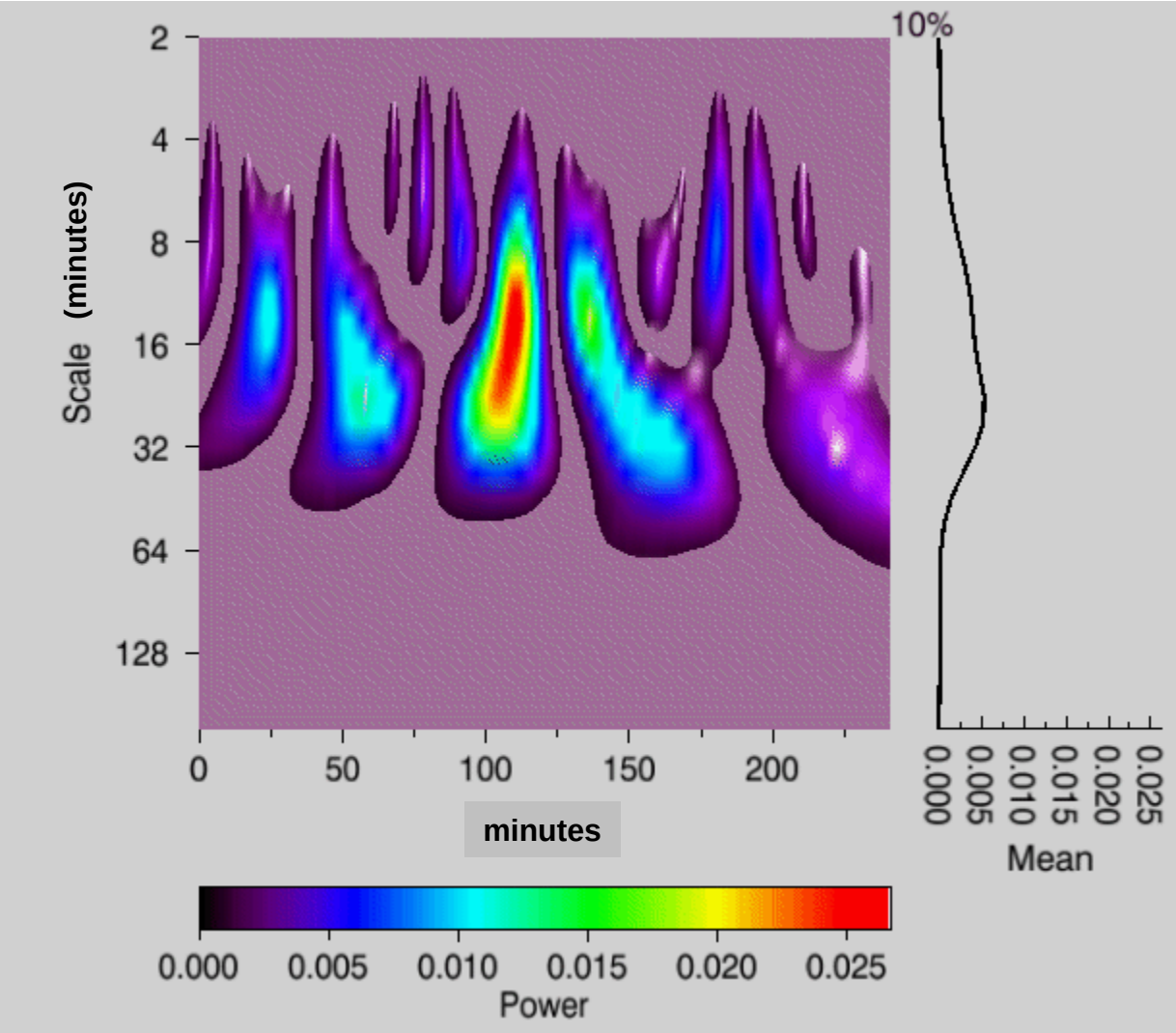
Scale (minutes)
2
4
8
16
32
64
128
0
50
100
150
200
minutes
10%
0.000
0.005
0.010
0.015
0.020
0.025
Mean
0.000
0.005
0.010
0.015
0.020
0.025
Power

d)

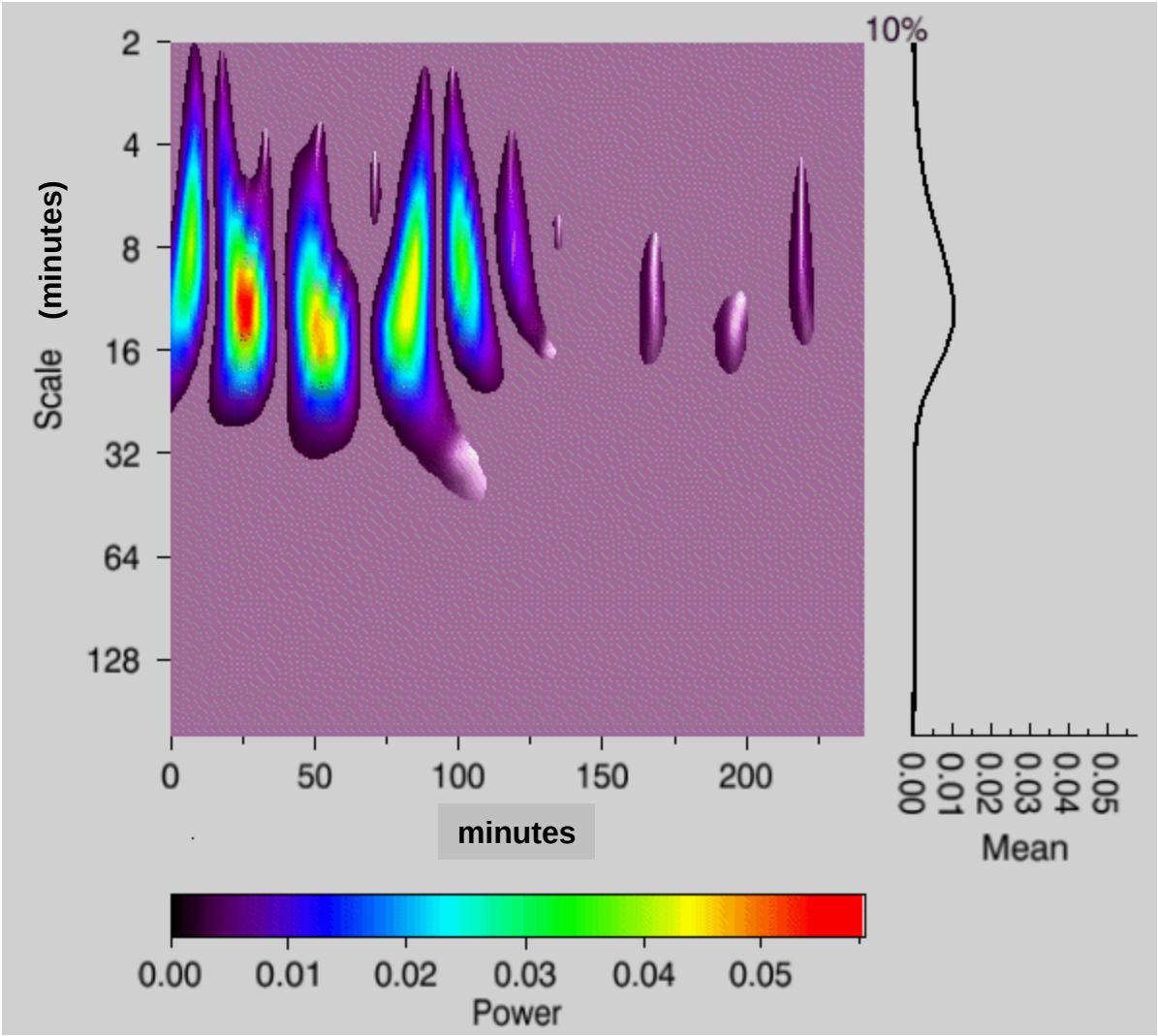
10%
Scale (minutes)
2
4
8
16
32
64
128
0
50
100
150
200
minutes
0.00
0.01
0.02
0.03
0.04
0.05
Mean
0.00
0.01
0.02
0.03
0.04
0.05
Power